RSC Advances

PAPER

View Article Online
View Journal | View Issue

Cite this: *RSC Adv.*, 2022, **12**, 29734

Study of molar properties of GO after doping with transition metals for photodegradation of fluorescent dyes†

Krishan Kumar, Riddhi P. Dave, Sachin Dev and Man Singh *

We synthesized graphene oxide (GO) doped with transition metal ions and characterized it using XPS, FT-IR, TGA/DTG, XRD, SEM, AFM, ICP-OES, UV/vis, and Raman spectroscopy. An intrinsic viscosity [η] of 0.002–0.012 g% @ 0.002 aq-GO was determined for viscosity average molecular weight (M_v) of GO at 288.15, 298.15, and 308.15 K. Mark–Houwink (M–H) constants k ($cm^3\ g^{-1}$) and a ($cm^3\ mol\ g^{-2}$) were calculated for 5–15 mg/100 mL polyvinylpyrrolidone (PVP), using 29, 40, 55 kg mol^{-1} as markers for calculating M_v by fitting the [η] to the Mark–Houwink–Sakurada equation (MHSE). We obtained 48 134.19 g mol^{-1} M_v at 298.15 K, and the apparent molar (V_{ϕ_m}, $cm^3\ mol^{-1}$), limiting molar volumes $(V^0_{GO})_{G\bar{O}0}$, enthalpy (ΔH_m, J mol^{-1}), entropy (ΔS_m, J $mol^{-1}\ K^{-1}$), viscosity (η_m, mPa s mol^{-1}), surface tension (γ_m, mN m^{-1} mol^{-1}), friccohesity (σ_m, scm^{-1} mol^{-1}), fractional volume (ϕ_m, cm^3 mol^{-1}), isentropic compressibility ($K_{s\phi,m}$, 10^{-4} cm s^2 g^{-1} mol), infer GO molar consistency throughout the chemical processes. Molar properties (MPs) infer a GO monodispersion producing negative electrons (e^-) and positive holes (h^+) under sunlight. The transition metal ions (Fe^{2+}, Mn^{2+}, Ni^{2+}, Cr^{3+}, TMI) doped onto GO (TMI-GO), can photodegrade methylene blue (MB) in 60 min compared with 120 min using GO alone. The 4011 C atoms, 688 hexagonal sheets, 222 π-conjugations, and 4011 FE were calculated from the 48 134.19 g mol^{-1}. The functional edges are the negative and positive holes generating centres of the GO 2D sheets.

Received 8th July 2022
Accepted 23rd August 2022

DOI: 10.1039/d2ra04230d

rsc.li/rsc-advances

Introduction

The M_v molar property of stoichiometric transition metal-doped 2D graphene oxide (TMI-GO) is a potential measure for the photocatalytic properties of fluorescent dyes. GO is widely used in the design of energy storage, telecommunication network, and solar energy functional materials.[1] However, to date no GO molar ratio driven approach has been adopted. TMI-GO works as a photocatalyst by capturing photons ($\hbar\nu$) from sunlight to generate electrons (e^-) and holes (h^+) resonating with the same frequency as a dye, to which they transfer energy, this photonic energy – mobile electrons – reduces the dye. Molar activities are not applicable unless M_v is determined, so the activities of GO with unknown M_v cannot widen applications on a molar scale.

GO could efficiently photodegrade polluting effluents in energy storage systems, if the TMI-GO e^- and h^+ energy corresponds. The size and surface charge of GO and TMI-GO affect wavefunction (ψ), so M_v needs to be a single mole of GO in a 2D sheet which remains fairly stable. The M_v depicts the alignment of holes to generate redox cycles. TMI-GO interfaces are recyclable photocatalysts with robust redox cycles as TMI and GO have close electronic clouds which retain their intrinsic activity.[2] The GO molar activities have never been focused on for molar photodegradation efficiency, so M_v is needed. Monodispersed GO is a viable route for balancing the cohesive and adhesive forces (cohad) without restricting orientations. Fluid and static dynamic activities of GO have been interfaced to determine the M_v using a survismeter at normal temperature and pressure (NTP).[3] GO sheets of different sizes were streamlined on capillary flow; as orientations may be faster or slower. So, a viscous flow time was averaged to determine [η]. The values of [η] consider a contribution of a certain sheet size, as the ultrasensitive GO sheets at boiling point for M_v determination, could damage the photocatalytic ability. Thus, M_v could help in the design of efficient solar cells, light emitting diodes, piezoelectric sensors and oscillatory sensors.[4,5]

Solid exfoliated photocatalyst GO sheets are efficient but are still limited to h^+ and e^- generation compared to higher surface areas with infinite redox cycles. Molar GO could be doped with heterocyclic compounds and transitional metal sulfide nanoparticles to study molar interfacial activities.[4,5] The photocatalytic activities of TMI-GO are high for the degradation of methylene blue (MB), and could be used to disintegrate this polymeric waste material into smaller alkyl chains to synthesize petrol and diesel.[6]

School of Chemical Sciences, Central University of Gujarat, Gandhinagar Sector-30, Gujarat, 382030, India. E-mail: Krishan8053649040@gmail.com; riddhidave15@outlook.com; sachin.dev708@gmail.com; mansingh50@hotmail.com

† Electronic supplementary information (ESI) available. See https://doi.org/10.1039/d2ra04230d

TMI-GO resonating holes in the same phase offer a new dimension of photocatalytic chemistry. The molar activities advance dispersion, surface area, and surface charges based on M_v for energy storage per mole, contrary to per gram. Large 2D laminar sheets as per M_v, affect quantum yield (Φ) of TMI-GO unlike a packed sheet with stronger van der Waals forces. The M_v of GO determines adsorption per mole of heavy metals, colourants, cancerous biodegradable wastes for *in situ* photodegradation and adsorption.[6] The M_v could revolutionize size dependent design of single, double and multiwalled carbon nanotubes.[2] Cannon–Brookfield–Ubbelohde viscometers measure the viscosity of aq-GO sensitive aq-solution without pressure equilibrium. A pressure equilibrium with a flow of 2D-GO nanothin laminar sheets may get partially folded by the cohesive forces. The survismeter with a dual force mechanism can measure the $[\eta]$ by considering cohesive as well as adhesive forces for M_v. Utracki *et al.* determined k and a constants from $[\eta]$ of 6 to 6000 kg mol^{-1} polystyrene in cyclohexane by mol. wt. of the macromolecule.[7] Dohmen *et al.*[8] determined the $[\eta]$ for 200 to 1000 g mol^{-1} polyethylene glycol in a homologous series of primary alcohols – acetone, and toluene at 298.2 to 323.2 K. Sadeghi *et al.*[9] reported the smallest effect of temperature on mol. wt., but GO is electronically sensitive and robustly responds to temperature variation. This mechanism has never been investigated as no M_v for GO has been reported. The k and a from $[\eta]$ values of aq-polyvinylpyrrolidone (PVP) for 10 kg mol^{-1} are reported for a mol. wt. of small-size macromolecules, but the M_v of GO has never been reported at 298.15 K.[10,11] No markers for k and a have been reported yet for desirable levels of aq-PVP; the $[\eta]$ is temperature dependent so k and a values vary at each temperature. Currently, g% is used to calculate molar properties (MPs) which could not provide information on molecular size *vs.* photocatalytic activity. Restrictions surrounding g% have obstructed the study of MPs despite high reproducibility and accuracy (Table 1).

Here, the molar size and surface area are used to design and develop wider GO applications. The M_v analyses of GO molar activities could be used for electrolyte, dendrimer, or ionic liquids for quality products and energy storage. Now M_v, *vis-á-vis* the stoichiometry of oxidizing mixtures and corresponding steps to synthesize GO of specific size, could be a new standard. This paper is a novel study on the chemistry of GO as a photocatalyst, including number of carbon atoms, pi conjugation, and number of functional edges, by determining the molar mass of GO. These studies are reported for the first time and are supported with physicochemical properties to evidence molar consistency during the chemical processes.

Table 1 Molar properties of GO in the literature

	Comparison		
Molar properties	Our studies	Ref.	Mol. wt.
Surface tension	Yes	27–33	No
Viscosity	Yes	28,32–40	No
Intrinsic viscosity	Yes	No	—
Friccohesity	Yes	38	No
Isentropic compressibility	Yes	No	No
Fractional volume	Yes	34–36,41	No
Entropy	Yes	4,25	No
Enthalpy	Yes	4,25,42,43	No
Gibbs free energy	Yes	4,25,42,43	No
Mol. wt. of GO	Yes	No	—
Apparent molar volume	Yes	No	—

Experimental section

Materials and method

Graphite (Gt) flakes, H_2SO_4 (98%), H_3PO_4 (85%), H_2O_2 (30%) $AgNO_3$, MB, $CrCl_3$, $MnCl_2$, $FeCl_2$, $NiCl_2$, and PVP (29, 40, 55 kg mol^{-1}) were procured from Sigma-Aldrich; $KMnO_4$, NaCl, and HCl (36%) from Rankem; petroleum ether (40–60) from SRL; absolute alcohol from Scvuksmandli Ltd India. The chemicals were used as received and the solutions were prepared in Milli-Q water of 0.5 $\times$ 10^{-7} scm^{-1} conductance.

Synthesis of GO from Gt

GO was synthesized with a mixture of H_2SO_4 and H_3PO_4 in an 8.5 : 1.5 ratio, this mixture was poured dropwise into 500 mL RB flask containing Gt and $KMnO_4$ in 1 : 6 ratio (9 g) kept on an ice bath. The suspension was kept for 30 min at room temperature (RT) and was refluxed for 12 h at 650 rpm at 55 °C. Ice-cold water and 3 mL H_2O_2 were mixed in a reaction mixture to cease the reaction.[4] The resultant product was centrifuged at 8000 rpm for 10 min and was washed with water and (5%) HCl alternately until the supernatant attained pH 7. The final washing was done with absolute alcohol. $AgNO_3$ and $BaCl_2$ tests ensured the complete removal of NaCl and Na_2SO_4 after washing. A cake-like brownish sediment was coagulated with petroleum ether and extracted in a Petri dish and dried at 60 °C for 24 h. GtO was exfoliated with minimum water by sonicating @ 28 kHz for 3 h to disrupt ABAB sheet stacking so a brownish GO was obtained (Fig. 1).

GO doped with TMI *via* photonic energy in sunlight

Transition metal salts ($CrCl_3$, $MnCl_2$, $FeCl_2$ and $NiCl_2$) were mixed with GO in a 1 : 4 ratio in a glass tube kept in sunlight for 90 min. The resultant material is noted as the TMI-GO template which settled at the bottom. The template was washed with water 2–3 times to remove unused TMI and GO. The $AgNO_3$ test ensured the complete removal of Cl^- ions. The TMI-GO was

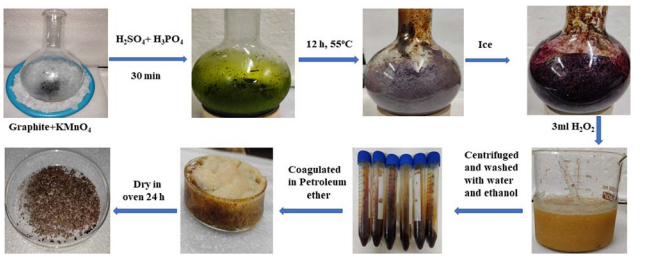

Fig. 1 GO preparation in the continuous process.

dried in a vacuum oven for 3 h at 50 °C to produce the powder form for use in the MB photodegradation.

Characterization

UV/vis spectra were recorded with Shimadzu UV1800 double beam spectrophotometer. X-ray diffraction (XRD) spectra were recorded on a Bruker Advance-D8 diffractometer with CuKα radiation ($\lambda = 0.15406$ nm, 40 kV, 40 mA). Thermal stability was determined using thermogravimetric analysis (TGA) in a N_2 environment on a EXSTAR TG/DTA 7300 analyzer. Functional groups were analyzed with an FT-IR spectrometer (PerkinElmer, Spectrum 65). Morphology and size were recorded using scanning electron microscopy (Zeiss Sigma 300) and atomic force microscopy (AFM5100 N). X-ray photoelectron spectroscopy (XPS) was performed at RT at $\sim 10^{-9}$ mbar with the help of hemispherical electron energy analyser (Phoibos 100 from Specs GmbH) and a non-monochromatic AlKα (1486.6 eV) laboratory X-ray source. The molar properties were measured using a Mansingh survismeter (Cal. 06070582/1.01/C − 0395, NPL, GOI).

Results and discussion

X-ray diffraction of GO and Gt

XRD elucidates the lattice of GO at $2\theta = 6°$ with a broad peak at an intensity of 2735 cps, and $2\theta = 8.85°$ with a sharp peak at an intensity 6900 cps (Fig. 2, black line). The mean free path is decreased at $2\theta = 6°$ as electron–electron repulsion occurs with a lower intensity, but upon sheet aligning at 0.997 nm it is increased.

A separate sheet supports unhindered hole generation for better photocatalysis. The nascent O atom with two lone pairs of electrons intercalates with the Gt layer to form GO. XRD of Gt is depicted at $2\theta = 26°$ with $d_{200} = 0.342$ nm intersheet distance with a mild lattice (Fig. 2, green line), supported by TGA at 193 °C.

Thermogravimetric analysis (TGA) and differential thermogravimetric (DTG) analysis

Stacking of GO sheets compared to strongly packed Gt with strong binding forces, have specific latent heat which can be studied using wt loss. Fig. 3 depicts GO decomposition in two steps: as a rapid wt loss >RT with 18% at 136 °C and a major 82% wt loss at 193 °C due to the removal of thermally labile oxygen containing functional groups (–O–, –CHO, >CO, –COOH, –OH). These have almost the same heat capacity generating the ψ in a similar phase to that adsorbed by TMI. The 82% of GO decomposed sharply at 193 °C, unlike the broader curve at 136 °C on removal of adsorbed atmospheric gases and water: the oscillatory activities with similar ψ weaken the covalent bonding of the carbon skeleton. The sharper transitions infer crystalline exfoliated GO sheets with almost the same functional edges, unlike the 18% wt loss from 50 to 136 °C, due to expulsion of the attached water molecules. These water molecules develop a unique rheology without damaging the sheet during fluid dynamics or friccofluidics acting as a shock absorber in regard to a 'lacey' GO sheet.

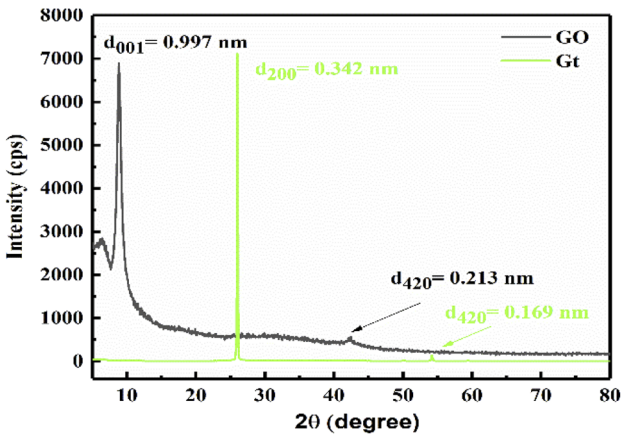

Fig. 2 XRD of GO and Gt with intersheet distance.

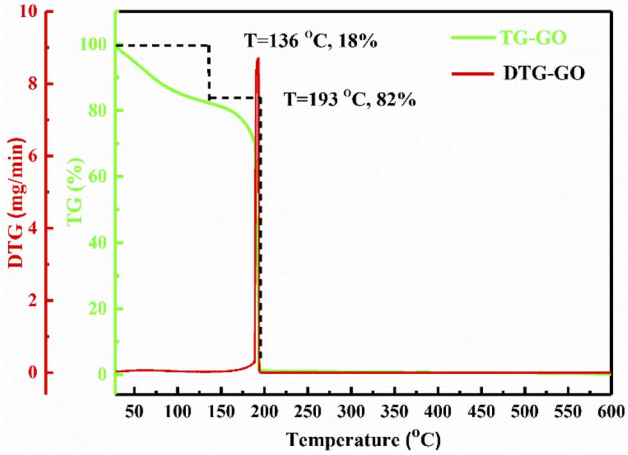

Fig. 3 TGA and DTG of GO with a prominent transition at 193 °C.

Such interstitial linkages of water protect the GO sheets during the fluid dynamic experiments using a survismeter, unlike with BP, LC-MS, and MALDI TOF. The interaction between electrostatic dipoles (ED) with FE of GO as GO-FE-ED-H_2O template bind the water dipoles strongly. The water does not obtain adequate energy to escape, unlike the O atoms of the functional groups upon a regular heating, where the sheet–sheet van der Waals forces are zero. The aqueous solutions of GO and TMI-GO remain stable and have reproduced the viscosity, surface tension and density primary data over 3 months. The reproduced primary data infer the structural stability. The GO and TMI-GO in solid states are fairly stable as studied using wt losses. The major wt losses of 82, 29, 45, 60 and 71% are at 193, 750, 345, 342 and 356 °C for GO, Cr-GO, Mn-GO, Fe-GO, and Ni-GO, respectively. These substances are non-hydroscopic and non-oxidizable with atmospheric air. The aqueous solutions of GO and TMI-GO were individually prepared at NTP, which remained monodispersed without coagulation or nanoclustering. These features inferred their stability even in aqueous solutions. Their stability in aqueous solutions was verified using aqueous solutions to photocatalyze MB in sunlight (SL), their molecular structures interacted with

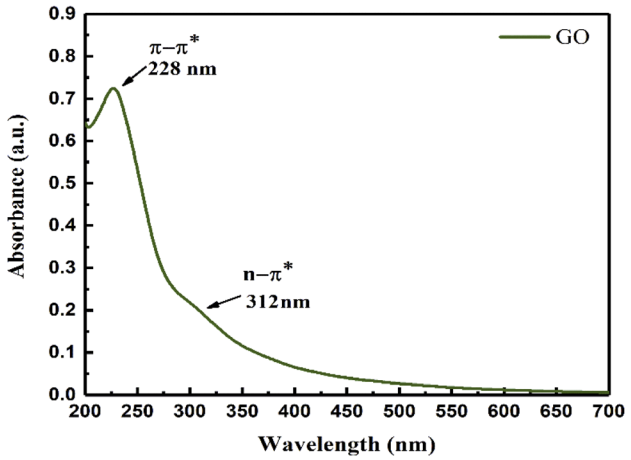

Fig. 4 UV/vis spectra of GO.

photons for photocatalysis. Thus, the photocatalytic reduction (PCR) and adsorption of the dyes authenticate their stability.

A sharper decomposition infers a single crystal lattice with accurate M_v following a Newtonian liquid. The functional edges of GO orient with different energies and stronger optimization at 193 °C (Fig. 3). GO and TMI-GO both respond to photons of sunlight as their functional edges are electronically sensitive with UV/vis, light. The sharper λ_{max} infers the holes interact while the C-skeleton with h^+ and e^- excite the electrons of O to oscillate. The electrons of O and the holes with induce a maximum electron–electron repulsion resulting in mild collisions as the wavefunction of the electrons harmonize.

UV/vis analysis

The broad UV peak with GO and O bonding at 312 nm infers a uniform O symmetric C-skeleton. The $\pi \rightarrow \pi^*$ transition of the hexagonal GO sheet oscillates at 8.718×10^{-19} J compared to 6.371×10^{-19} J for the $n \rightarrow \pi^*$ of the O atom. These infer an effective response of photons where GO interacts with sunlight (ESI, Fig. 3.5†). The $\pi \rightarrow \pi^*$ of GO and $n \rightarrow \pi^*$of the O atom of (–COOH, >CO, –CHO, –OH, –O–) oscillate in the same phase. The active sites contribute to disperse water on GO for accurate M_v (Fig. 4).

Scanning electron microscopy (SEM)

The lacey GO 2D sheet holding various functional groups is realigned to stack that gained a thickness. The different stacking patterns are analysed with SEM micrographs, for its analysis, the sample uniformly was spreaded on carbon tape and mounted on the stub stuck of the equipment. Inside the coating chamber, plasma sputtering was directed on a stub, targeting Au and Pd in a 80 : 20 ratio for coating. After coating, a 7 kV beam stimulated the secondary electrons from the GO surface. GO morphology is rough, furrowed multiple layers or ripples with the stronger H-bonding between the multiple successive layers of GO. Fig. 5 shows the pattern of monodispersed lacey GO sheets with a higher surface area. The GO sheets are

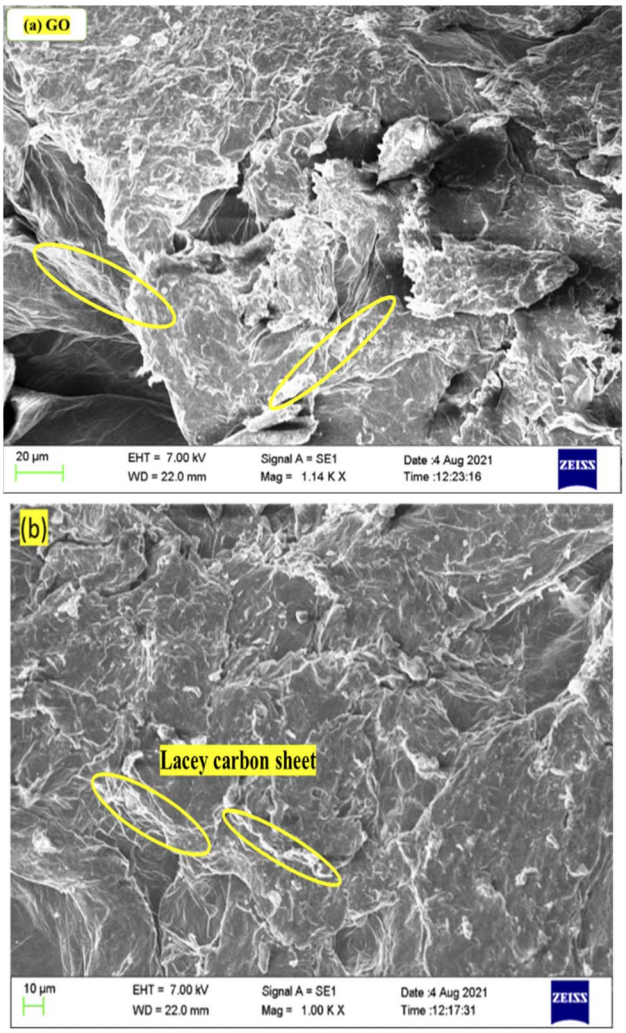

Fig. 5 SEM of GO (a) 20 µm and (b) 10 µm, infer laminar sheets of lacey carbon.

stacked, however, they seem to be of equal size and dimension, optimized with functional groups at specific stretching frequencies.

FT-IR analysis

FT-IR stretching frequencies *via* Fourier transform at similar frequencies depict the specific spatial alignment at a close interface. The spatial arrangements are optimized but the stretching intensity causes the internal morphology to optimize as sheets, as the density of –O–, –CHO, >CO, –COOH, –OH increases (Fig. 5). The stretching frequencies of –COOH, >CO, –CHO, –OH, –O– at wavenumber ($\bar{\nu}$)[6,12] and their transmittance bands, infer bond energies.[13] The broad peak at 3351 cm^{-1} is due to the –OH of water bonding on the GO surface. The –O–, –CHO, >CO, –COOH, –OH give IR bands at 1071, 1400, 1250, 1750, 1626 cm^{-1}, respectively (Fig. 6).[12,14] The symmetric stretching alignment with stable dipoles and higher polarizability which stack to develop the topographic surface, are illustrated with Raman spectroscopy and AFM.

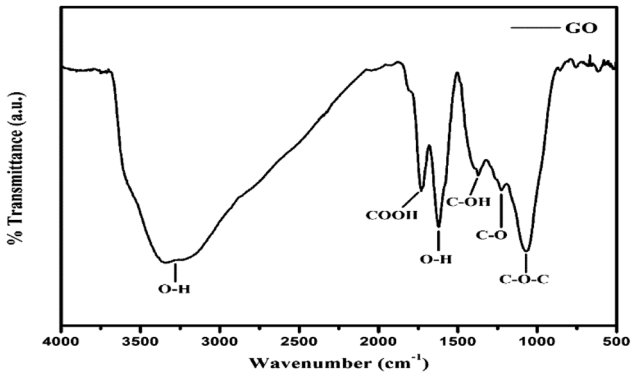

Fig. 6 FT-IR spectra of GO containing oxygenated functional groups.

Atomic force microscopy (AFM)

AFM was carried out on a 1 × 1 cm thin film of GO on silica wafer using a non-contact mode for capturing the surface morphology and thickness. AFM shows the topography of ~1.05 nm thick single layer and complete GO exfoliation, in agreement with the literature.[15–17] AFM infers topography with ~1.05 nm thick single layer individual GO sheets, in agreement with the literature.[15–17] The soft GO sheet has wrinkles and overlaps that are optimized by the sheet density of state. The number of sheets in a specific area infer their stacking as a single layer of ~1.05 nm thickness, whereas the remaining sheets correspond to multilayer GO stacks (Fig. 7a–c). The standard preparation protocol enabled the exfoliation of individual GO sheet stacking, harmonized along the *z*-axis with multiple restricted splits (Scheme 1).

The 2D GO nanosheets have been stacked next to each other due to weak van der Waals forces as the sheets have (–COOH, CO, –CHO, –OH, –O–) functional groups, along with the active functional edges. These chemical species have active surface charges that interact and lead to the stacking of the GO sheets along the *z*-axis. This stacking is not compact, and is rather loosely bound and develops adequate h^+ and e^- holes. Hence, these functional moieties of the 2D GO sheets align the individual sheet *via* stacking. The furrows and ridges are seen in the topography of the GO sheets which infer the equal distribution of the stacked sheets with weak cohesive and adhesive forces. These activities are properly explained by the friccohesity data (Tables 16–18). Photons can easily enter the stacks or furrows (Fig. 7). The furrows are almost equally distributed as the *z*-thickness of the adjacent furrows is almost equal. Hence these are synchronised and integrated as a single unit of 96.5 nm height within 400 nm. These data further evidence the porosity of the GO sheets needed for PCR (Fig. 24).

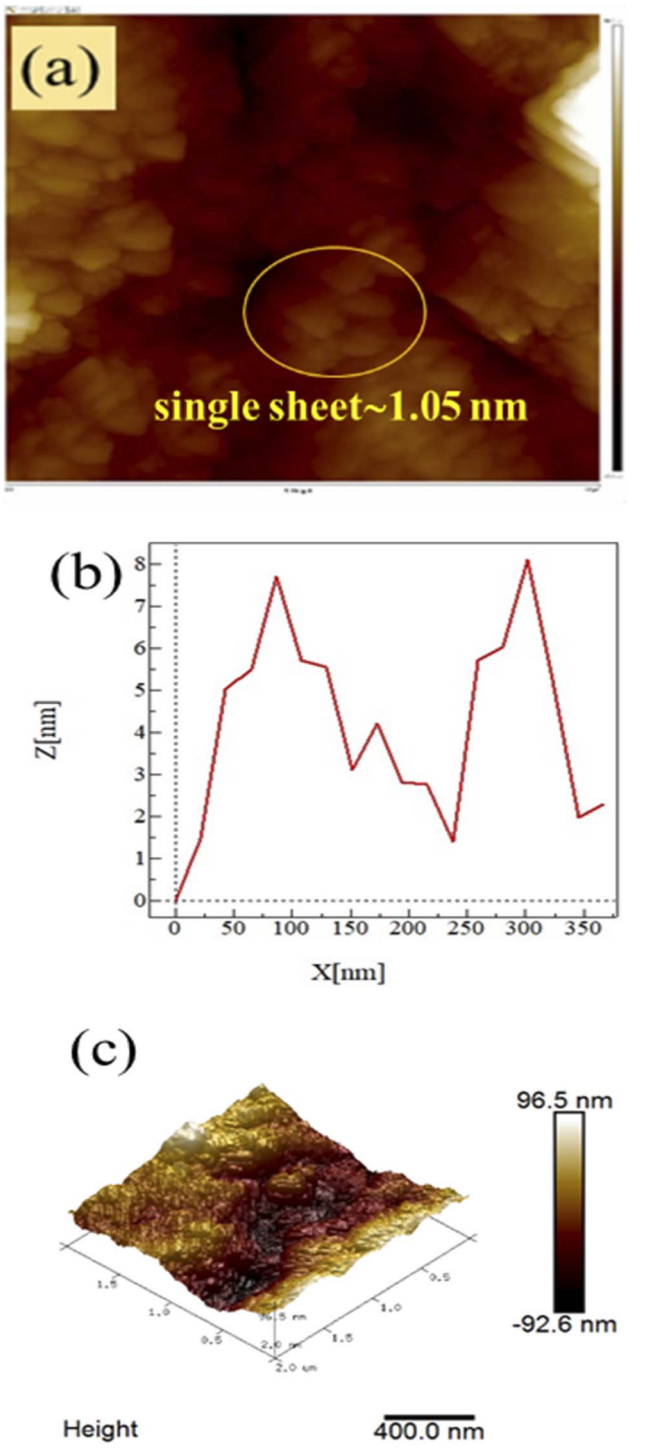

Fig. 7 (a) Inferred surface morphology, (b) *z*-axis, and (c) 3D image, of GO.

Raman spectroscopy analysis

Raman analyses $I_D/I_G = 0.91 < 1$ of D (deformed) and G (symmetric) bands with intensities of 3800 and 4200 cps, as G > D shows symmetric deformation on the GO sheet. The intensities at specific shifts provide information on the defects, crystalline structures, and alignments on GO.[18] The D, G and 2D peaks at 1355, 1599 and 2924 cm^{-1}, respectively, correspond to sp^2–sp^3 C–C stretching, and the (I_D/I_G) intensity ratio shows the disorder of a sheet.[19]

The Raman spectra infer 1st order scattering of the E_{2g} phonon from sp^2 C atoms causing a G band at 1599 cm^{-1} and a *k*-point breaking of the A_{1g} symmetry. The reduced 2D intensity infers modulated bumps due to minor reorientation, which

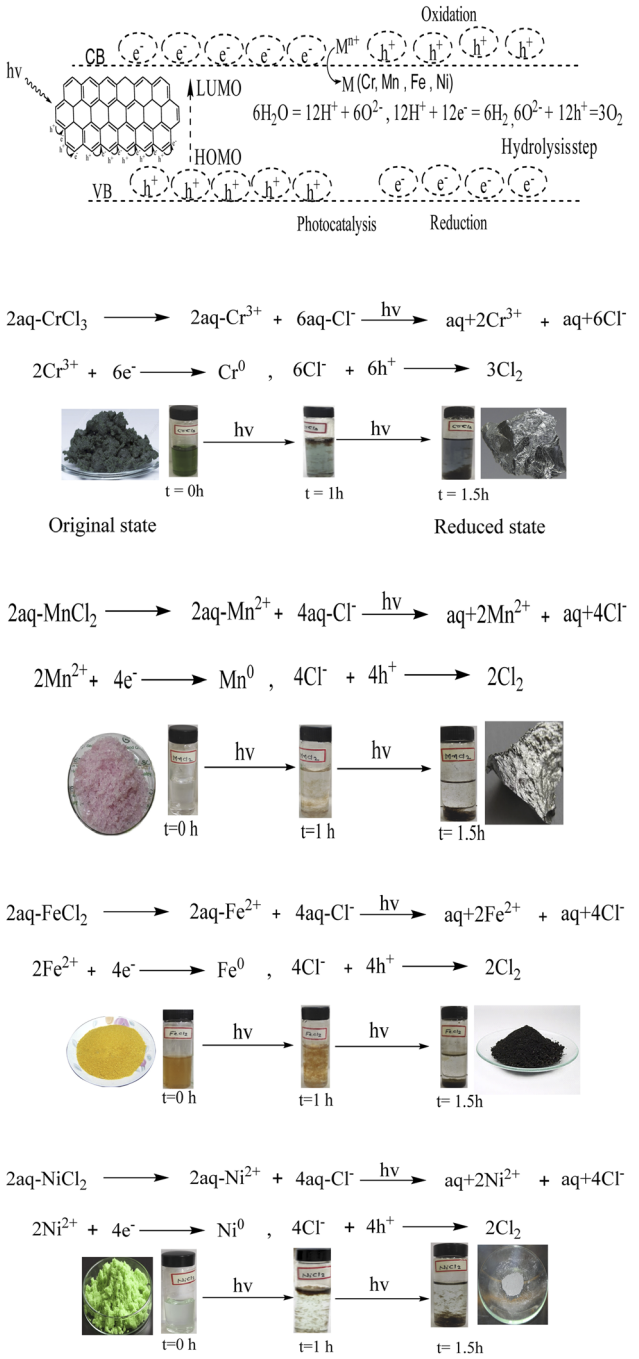

Scheme 1 GO doped with TMI.

is a competing mechanism where the defects increase with intensity of the G band. The number of defects controlled by ultrasonication time induced the D band at 1355 cm^{-1}, where $I_D/I_G < 1$ infers fewer defects[6,20] and 2D layer formation (Fig. 8). The split shows that there are deep furrows and upward ridges with almost symmetric surface topography, which allows weaker van der Waals forces to receive photons for hole generation. The stretching of the O atom bonds of the functional groups differ from those of the C atoms of GO (Fig. 6). The 0.002 g% aq-GO was boiled for 45 min compared to 25 min

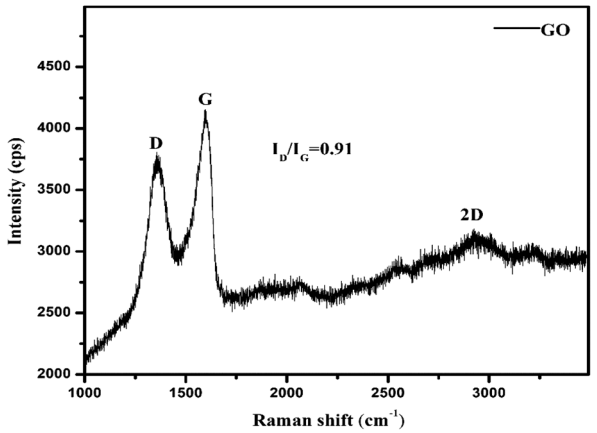

Fig. 8 Raman spectra of GO.

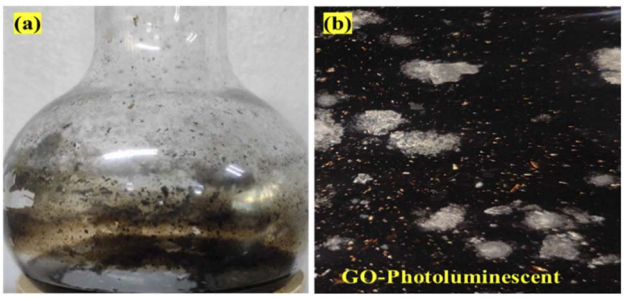

Fig. 9 (a) Formation of GO thin sheet and (b) photoluminescent-GO nanoclusters.

for the same amount of water with similar heating. The 0.002 g% aq-GO was cooled to RT and kept for 24 h, the thin GO sheet and gold-colour photoluminescent nanoclusters were grown and scintillated under visible light with a sharper reflection (Fig. 9). The boiling separated the rGO fragments out of the aggregated nanocluster at RT. GO sheets surrounded by H_2O molecules restrict the GO–GO alignment in the *z*-axis, as hydrogen bonded water inhibits GO downward movement, and air pressure restricts upward growth. The surface of structured water acts as a sliding surface for GO–GO growth in the *xy* plane. The 2D sheet has a *z*-axis at least, while agglomerated 3D nanoclusters initiate secondary transitions as phosphorescence. The water dipoles within an intersheet could have kinetic and potential energies as per the Schrödinger equation.

$$E\psi = \left(\frac{P^2}{2m} - \frac{q^+q^-}{4\pi\varepsilon_o r}\right)\psi \text{ and } \frac{\partial}{\partial t}\left(\frac{q^+q^-}{4\pi\varepsilon_o r}\right) \cong 0 \qquad (1.0)$$

Kinetic energy ($p^2/2m = 0$) at NTP does not generate holes within the valence and conduction bands, so there are zero changes in wavefunction as no change in eigenvalue *E* and eigenfunctions ψ occurs in the photocatalysis timeframe. The dipoles of water oscillate beyond the potential energy, and the functional edges with h^+ and e^- charges interlink the water and

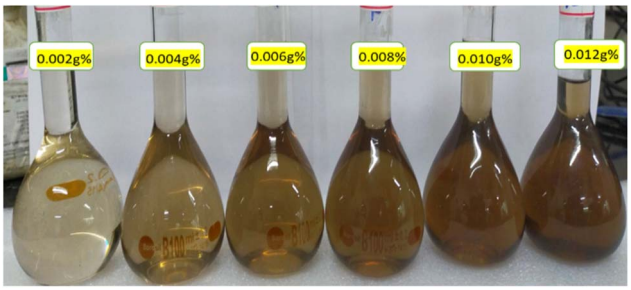

Fig. 10 GO solutions at different viscosity to investigate molar properties.

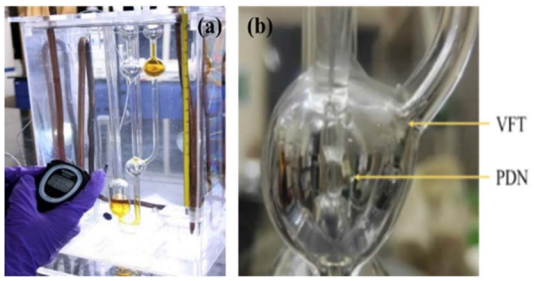

Fig. 11 (a) Sample inserted in survismeter, (b) GO solutions orientation in the capillary.[24]

GO together. Thus, the surface energy explains these energy linkages.

Calculations and sample preparation for the molar properties of GO

Calibration of PVP marker to determine M–H constants. The M_v is calculated using calibration constants with 0.005–0.015 g% @ 0.005 g% of 29, 40, and 55 kg mol^{-1} PVP marker to determine viscosity. The viscosity of 0.002–0.012 g% aq-GO @ 0.002 g% were measured in the dark at 288.15, 298.15, and 308.15 K (Fig. 10). The H_2O adhering to GO influenced the viscous flow time on reorientation, forming pendant-like drop out due to the cohesive and frictional forces. The functional edges deformed irreversibly, so a survismeter for measuring viscous flow time and pendant drop number was used. Samples were lifted from the reservoir bulb to the buffer bulb of the capillary under reduced pressure avoided mechanical shocks. The sample equilibrated in the buffer bulb for 3 min and was allowed to backward flow, a CPU (controlled pressure unit) facilitates a hassle-free capillary flow (Cal. 06070582/1.01/C – 0395, NPL, GOI).[21] The M–H constants infer size and PVP interactions with specific rheology at a constant temperature with ±0.01 °C and ±0.1 × 10^{-5} g analytical balance (Table 2). The GO was added to an RB flask with Millipore water and equilibrated for unhindered fluid flow. The survismeter was calibrated with aq-NaCl, and closely agrees with the literature (Fig. 11 and ESI Tables 4.1–4.3 and 5.3–5.5†).

Table 2 Mark–Houwink constants

T (K)	k (cm^3 g^{-1})	a (cm^3 mol g^{-2})
288.15	2.611 × 10^{-10}	2.1534
298.15	6.500 × 10^{8}	−1.7264
308.15	4.7953 × 10^{-4}	0.8465

Viscosity (η, mPa s). η was calcu!–lated using eqn (1.1)

$$\eta = \left(\frac{t}{t^{o}}\right)\left(\frac{\rho}{\rho^{o}}\right)\eta_0. \quad (1.1)$$

From the density (ρ) of aq-GO and the η_0 and ρ^{o} of water, relative viscosity (η_r) is derived as:

$$\eta_r = \left(\frac{\eta}{\eta_0}\right)_T \quad (1.2)$$

and

$$\eta_r = 1 + 2.5\phi \text{ and } \phi = \frac{4}{3}\pi r^3 N_A c. \quad (1.3)$$

The η_r is fitted using eqn (1.3) for $[\eta]$ (Fig. 12(a and b), Tables 16–18 and ESI, Table 5.2†).

Surface tension (γ, mN m^{-1}). The γ was calculated using eqn (1.4)

$$\gamma = \left(\frac{n_o}{n}\right)\left(\frac{\rho}{\rho^{o}}\right)\gamma^{o} \quad (1.4)$$

where γ^{o}, n_o, ρ^{o} and γ, n, ρ are surface tension, pendant drop numbers (pdn) and density, of water and sample, respectively (Tables 16–18, and ESI, Table 5.2, Fig. 1.0†).

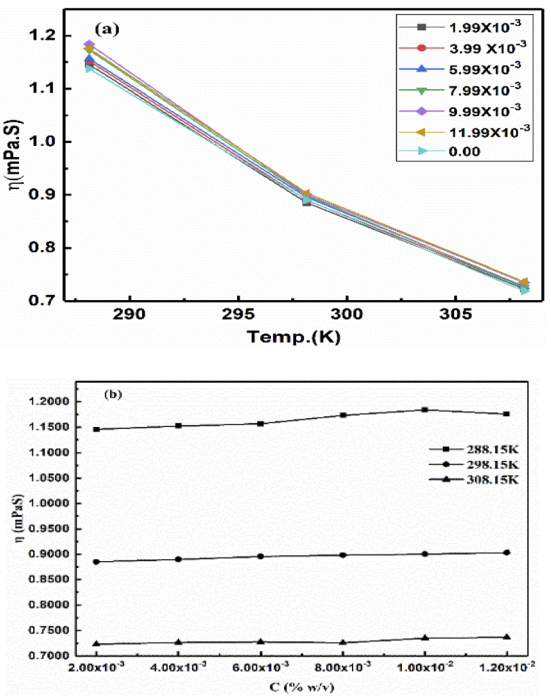

Fig. 12 (a) Viscosity *vs.* temperature, (b) viscosity *vs.* concentration.

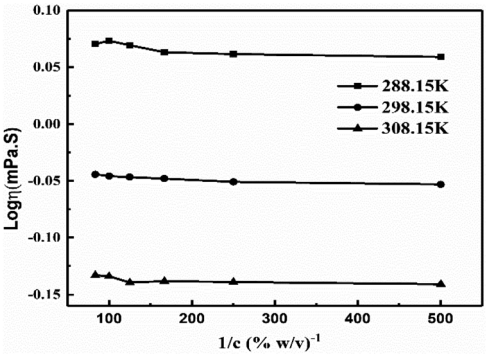

Fig. 13 The log η *vs.* 1/c for the activation energy of aq-GO.

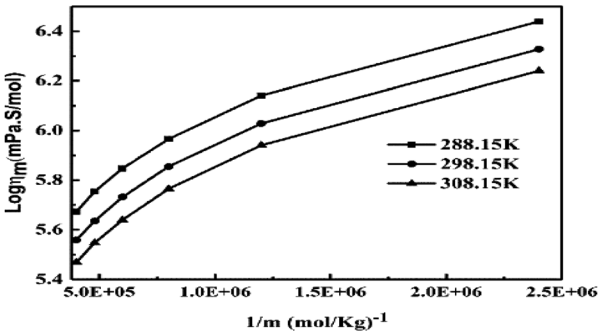

Fig. 14 log η_m *vs.* 1/m to calculate the molar activation energy (E_a) of aq-GO.

Friccohesity (σ, cm S^{-1}). The σ was calculated using eqn (1.5)

$$\sigma = \sigma^{o}\left(\frac{t}{t_0} \pm \frac{B}{t}\right)\left(\frac{n}{n_0} \pm 0.0012(1-\rho)\right)$$
$$\sigma = \sigma^{o}\left(\frac{t}{t_0}\right)\left(\frac{n}{n_0}\right) \text{ and } \sigma = \frac{\sigma^{o}}{t_0 n_0}(t \times n) \quad (1.5)$$

The σ and σ^{o} are friccohesity of solution and water, respectively; $\pm B/t$ kinetic and $\pm 0.0012(1-\rho)$ buoyancy corrections of 1×10^{-7} order are omitted; parameters for solvents are common and rationalized with the Mansingh constant (M_c).

$$M_c = \frac{\sigma^{o}}{t_0\, n_0} \quad (1.6)$$

Friccohesity infers a homogenized aq-GO by mutually exchanging the cohad forces that lower ΔE and show solvent adherence to GO. The quantum mechanically stabilized GO acts like quantum dots with zero conductivity, unlike aq-TMI-GO. The GO with functional edges resonates to transfer energy without a change in relaxation time or mean free path by avoiding aggregation (Tables 13–15). From these quantum controls we calculated the relative (σ_r), specific ($(\sigma_r - 1)/c$), and intrinsic $[\sigma]_{c\to 0}$ friccohesity (Tables 16–18, and ESI, Fig. 3.1, 3.3†). The E_a acquired from the medium reorients the functional edges *vs.* electrostatic dipoles, allowing energy equipartitioning that avoids spontaneous aggregation.

$$\eta = \eta_0 \frac{g e^{-\frac{E}{kT}}}{\sum g e^{\frac{E}{kT}}} \quad (1.7)$$

Table 3 log η *vs.* 1/c in Fig. 13

Regression constants		
T (K)	Intercept (mPa s)	Slope (mPa s g cm^{-3})
288.15	0.0810	−0.00010
298.15	−0.0400	−0.00006
308.15	−0.1294	−0.00006

Where η, η_0, g, and T are viscosity of solution, viscosity of solvent, degeneracy in the energy level, and temperature.

Activation energy (E_a, J mol^{-1}). The E_a is calculated by fitting η values with the Arrhenius eqn (1.8)

$$\eta = A e^{-E_a/Rc} \text{ or } \text{Slope} = -2.303\frac{E_a}{R},\ E_a = -\frac{\text{Slope} \times R}{2.303} \quad (1.8)$$

The data are given in Fig. 13 Table 3 and Fig. 14, Table 4 and ESI Table 5.0.†

Molecular weight (mol. wt., g mol^{-1}). The GO mol. wt. is calculated using $[\eta]$ and M–H constants with MHS eqn (1.9).

$$[\eta] = KM^{a} \text{ or } \log[\eta] = \log k + a \log M \quad (1.9)$$

Where $[\eta]$ is the intrinsic viscosity, M the mol. wt., k and a the M–H constants, when it is monodispersed in aqueous media similar to GO PVP (Table 6 and ESI Table 5.0†). The molar activities infer dispersion which are caused due to rotational, vibrational, electronic, and transitional motions of a molecule. These motions align the interacting constituitional units of a molecule to generate the molar volume. The M_v shows the E_{am} for mass transfer and a solvent adherence for viscous flow.

Apparent molar volume ($V_{\phi,m}$). The V_{ϕ_m} infers the strength of FE–ED interactions which show H_2O is an indispensable part of the GO net volume. The solvated GO V_{ϕ_m} is calculated by

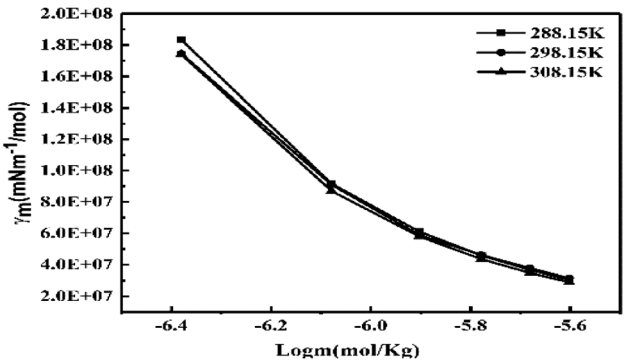

Fig. 15 γ_m *vs.* log m to see the molar surface excess concentration and calculate the surface area of aq-GO.

Table 4 The constants (a) log η_m *vs.* 1/*m* in Fig. 14; (b) γ_m *vs.* log *m* in Fig. 15, of aq-GO

Fig. 14, log η_m *vs.* 1/*m*			Fig. 15, γ_m *vs.* log *m*	
T (K)	Intercept (mPa s mol^{-1})	Slope (10^{-7}) (10^{-3} mPa s g^{-1})	Intercept (10^9) (mN m^{-1} mol^{-1})	Slope (10^9) (10^3 g mN m^{-1} mol^{-2})
288.15	5.3791	9	6	2
298.15	5.2580	9	6	2
308.15	5.1687	9	6	2

$$V_{\phi_m} = \frac{1000(\rho_0 - \rho)}{\rho_0 \rho m} + \frac{M_v}{\rho} \quad (2.0)$$

The ρ, m and M_v are density, molality and mol. wt. of GO, respectively, and ρ_0 is the density of water (Fig. 16a, Table 5, Tables 13–15 and ESI Fig. 1.6†).

Surface excess concentration (τ, mol cm^{-2}) and surface area ($1/\tau$ = cm^2 mol^{-1}). The τ and $1/\tau$ both infer an excess of GO gathered at the aq-GO surface as a continuous thin layer, calculated from the slope of dγ *vs.* log *c* with eqn (2.1),

$$d\gamma = -2.303RT\tau \log c, \ \text{slope} = -2.303RT\tau$$
$$\tau = \frac{\text{slope}}{-2.303RT}, \ \text{surface area} = \frac{1}{\tau} \quad (2.1)$$

where *R* is the gas constant and *T* is the temperature (see Fig. 19 below and 15 above, Table 6, and ESI, Table 5.0†).

Molar Gibbs free energy (ΔG_m). The ΔH_m and ΔS_m are calculated from η_m, *R*, *T*, and E_{am} (molar activation energy), to determine the disorder created per mole.

$$\Delta G_m = -2.303nRT \log(\eta_m) \ \text{and} \ E_{am} = \Delta H_m - 2.303RT,$$
$$\Delta H_m = E_{am} + 2.303RT$$
$$\Delta G_m = \Delta H_m - T\Delta S_m \ \text{and} \ \Delta S_m = \frac{\Delta H_m + \Delta G_m}{T} \quad (2.2)$$

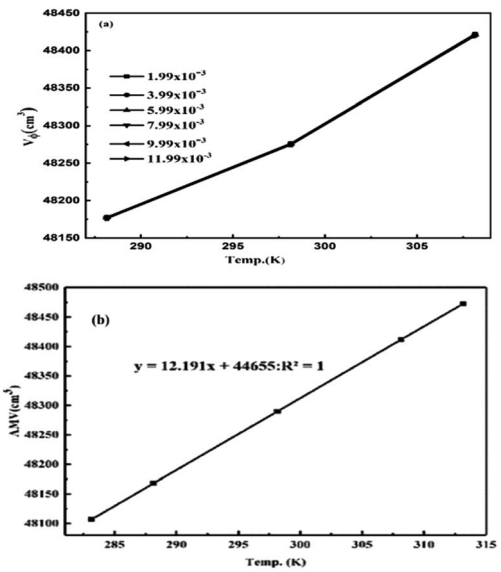

Fig. 16 (a) V_ϕ *vs.* temperature of aq-GO; (b) V^0_{GO} *vs.* temperature of aq-GO.

ΔG_m, ΔH_m, ΔS_m, are listed in Table 6 and ESI Table 5.0†.

Molar fractional volume (ϕ_m) and isentropic compressibility ($K_{s\phi_m}$). The ϕ_m and $K_{s\phi_m}$ both infer GO binding with H_2O molecules and are calculated as

$$\phi_m = \frac{\eta_r - 1}{2.5 \times m} \quad (2.3)$$

and

$$K_{s\phi_m} = \frac{1}{u^2 \rho \times m} \quad (2.4)$$

where η_r, *u*, ρ, and *m* are the relative viscosity, sound velocity, density, and molality (Tables 16–18, ESI, Fig. 1.8 and 2.1†).

Hydrodynamic volume (HDV). Molar radius (R_m) infers the number of the water molecules adhered to GO during viscous flow that create the HDV, calculated using [η]:

$$\text{HDV} = [\eta] \times M_v \quad (2.5)$$

and

$$R_m = \left(\frac{3\phi}{4\pi N_A m}\right)^{1/3}. \quad (2.6)$$

The ϕ, N_A, and *m*, values are listed in Table 13 and ESI Table 5.6 and 4.8.† The pressure was reduced in the capillary using

Table 5 The regression constant for V_ϕ *vs.* temperature in Fig. 16a and b

Fig. 16a V_ϕ *vs.* *T*/K			
S. no.	Conc. (10^{-3})	Intercept (cm^3)	Slope (cm^3 K^{-1})
1	2.00	44 648	12.224
2	4.00	44 656	12.192
3	6.00	44 651	12.210
4	8.00	44 656	12.191
5	10.00	44 649	12.212
6	12.00	44 655	12.191

Fig. 16b V^0_{GO} *vs.* *T*/K	
T (K)	V^0_{GO} (cm^3 mol^{-1})
283.15	48 106.88
288.15	48 167.84
298.15	48 289.75
308.15	48 411.66
313.15	48 472.61

Table 6 Molar parameters of GO at three temperatures[a]

T (K)	M_v	$1/\tau$ (10^{-6})	E_{am} (10^{-5})	ΔG_m (10^{-3})	ΔH_m (10^{3})	ΔS_m
288.15	46 886.03	−2.75862	−1.723242	−4.69086	−5.5172489	−19.147125
298.15	48 134.19	−2.85436	−1.723242	−4.75818	−5.7087204	−19.147126
308.15	42 845.25	−2.95010	−1.723242	−4.84116	−5.9001917	−19.147126

[a] Symbol: M_v = viscometric mol. wt. (g mol^{-1}), τ = surface area (m^2 mol^{-1}), E_{am} = molar activation energy (J mol^{-1}), ΔG_m = molar Gibb's free energy (J mol^{-1}) ΔH_m = molar enthalpy (J mol^{-1}), ΔS_m = molar entropy (J mol^{-1} K^{-1}).

Table 7 Internal parameters of GO sheets

M_v	# C-atom	# Hexagonal sheets	# π-conjugation	# FE
48 134.19 g mol^{-1}	4011	668	222	4011

a piston to transfer a sample to the respective unit. On opening a pressure limb, liquid in the reservoir bulb prevents air entry and abrupt jerking. Under reduced pressure, the streamlined GO has minimal relaxation time for high accuracy in M_v. The 102 and 103 °C boiling points of 0.006 and 0.008 g% aq-GO, respectively, compared to water at 100 °C infer water is binding to GO (Fig. 9). At 288.15 K, the GO acquired energy from the medium causing a drastic change in its reorientation from 0.006 to 0.008 g%, unlike 0.012 g% GO that gets saturated upon sonication @ 28 kHz, increasing viscous flows. The lower viscosity for aq-NaCl at 298.15 K compared to 288.15 and 308.15 K, infer ion dipole interactions (Table 7). The NaCl disrupts water, unlike aq-GO and aq-PVP but similar to exfoliated GO sheets.[22,23]

The M_v *vs.* photons studies that vary the GO molar concentration were attained and focus on photons per mole of GO at various pH and temperature. The molar photocatalyzing activities were explored to reduce the dyes and transitional metal salts (Table 8). The functional edges and electrostatic dipoles streamlined the aq-GO viscous flow in a uniform capillary.[25,26]

Monolayer water adhesion around GO spins are controlled by temperature as,

$$(E - E_F) = k_B T \ln\left(\frac{1}{f_i} - 1\right) \text{ (Fermi Dirac equation)} \quad (2.7)$$

where E overall energy (kinetic energy and potential energy), E_F Fermi energy, f_i occupancy of Fermi energy level, $T = 0$ gives $E = E_F$ unlike $E \neq E_F$ for 298.15 K. The aligned wavefunction coordinate PCR activities as,

$$E = KT = \frac{1}{2}mv^2 = \frac{\hbar c}{\lambda}, \quad E = \frac{P^2}{2m} = \frac{\hbar c}{\lambda}, \quad E = 8.718 \times 10^{-19} \text{ J}. \quad (2.8)$$

Where $T = 0$, the $E = kt = P^2/2m = \hbar c/\lambda = 0$ at $T > 0$, so the wavefunction is robust. The GO molecule being larger in size holds many functional groups with different electronic configurations holding different energies at the surfaces of the GO. The different surface energies oscillate with the different wavefunctions which generate the different orders of the energy. These are the disordered surfaces with different sets of entropies at a topography. The different entropies at the surface than the bulk states cause energies to be exchanged between the surface and the bulk states. This is described by the tentropy which becomes significant during the molecular interactions and photocatalysis. The k_bT (1.38×10^{-23} m^2 kg s^{-2} K^{-1} × 298.15) = 411.64 m^2 kg s^{-2} oscillates at 298.15 K with a gradient on its topographical entropy or tentropy. aq-GO has an enhanced equilibrium of cohesive *vs.* adhesive forces,

$$\frac{\partial \gamma}{\partial \eta} = \frac{\partial \text{HB}}{\partial \text{FE}} = \frac{\partial(\text{H}_2\text{O amount})}{\partial(\text{GO amount})} = \text{Cohad constant}. \quad (2.9)$$

Eqn (2.9) infers hydrogen bonding (HB) disruption to adhere to GO upon increasing η and decreasing γ, as the HB are released by weakening cohesive force and can adhere to the GO surface. Hence, a weaker cohesive force with lower γ allows adherence to the GO surface increasing shear stress (Fig. 17). M–H constants k and a, derive from $\ln[\eta]$ *vs.* $\ln M$, the higher viscosity values at 298.15 K decrease with M_v unlike at 288.15

Table 8 The parameters related to Φ for the reduction of MB through TMI-GO[a]

TMI-GO-MB	λ_{abs} (nm)	λ_{em} (nm)	E_{abs} (10^{-19}) J	E_{em} (10^{-19}) J	n_a (10^{14}) s^{-1}	n_e (10^{14}) s^{-1}	Adsorption (%)	Φ (%)
Cr ($4s^13d^5$)	663	668	2.9982	2.9757	4.52488	4.49102	85.67	99.25
Mn ($4s^23d^5$)	661	665	3.0073	2.9892	4.53858	4.51128	98.67	99.40
Fe ($4s^23d^6$)	665	668	2.9892	2.9757	4.51128	4.49102	98	99.55
Ni ($4s^23d^8$)	664	675	2.9937	2.9448	4.51807	4.44444	98.35	98.37

[a] Absorbed wavelength (λ_{abs}), emitted wavelength (λ_{em}), absorbed energy (E_{abs}), emitted energy (E_{em}), number of absorbed photons (n_a), number of emitted photons (n_e) and quantum yield (Φ).

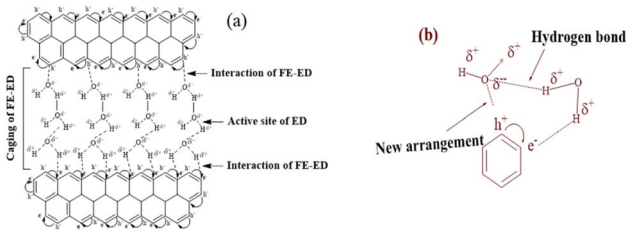

Fig. 17 (a) Interface of functional edges and electrostatic dipoles *via* monolayer hydration of the GO sheet, (b) sheet array with water influencing the fluid dynamics.

and 308.15 K. The viscosity values for aq-PVP at higher concentration are the same with almost a similar response at each temperature, this infers the presence of similar adhesive forces (Fig. 18 and Table 9). The GO has weakened the cohesive forces and strengthened the adhesive forces of H_2O as shown in the η_{sp}/C *vs.* temperature plots at 288.15 and 308.15 K (ESI Fig. 3.9†), which are close but differ at 298.15 K for 0.002–0.004 g%: the concentrations used produced closely placed $[\eta]$ values at 288.15 and 308.15 K, unlike 298.15 K due to a thermal alignment.

The η_{sp}/C values at 308.15 K, infer reorientation of the oppositely charged functional edges and electrostatic dipoles with GO–GO interactions at higher thermal energy by weakening their interactions. From 0.002 to 0.004 g% at 298.15 K increasing concentration weakens the interaction of the edges and dipoles with a stronger temperature effect (ESI Fig. 3.9†). The $\partial(\eta_{sp}/c)/\partial m$ infers a molar shift in interaction of edges and dipoles as a sensitive PCR *vs.* concentration dependence of the PCR sensor. The oscillatory arrays at 298.15 K equilibrate the interaction of the functional edges and electrostatic dipole monomer H_2O *via* cohad ↔ cohesive ± adhesive (ESI Fig. 3.9†). The γ values decrease on increasing concentration and temperature, both weakening the cohesive forces unlike the 0.012 g% at 288.15 and 308.15 K (ESI Fig. 1.0a and b†). Results from lower density at 308.15 K compared to 288.15 and 298.15 K, infer the weaker interaction of the edges and dipolar oscillation unlike a lower thermal energy. The closely placed density values infer the GO-FE-ED-H_2O template, as the interaction of edges and dipoles maintain similar adhesive forces on increasing temperature. The reproducibility of density values show the stability without clustering, due to the interaction of functional edges and electrostatic dipoles. The wavefunction of functional edges and electrostatic dipoles behave as a simple harmonic oscillator by transferring the energy at three temperatures (ESI Fig. 1.1†).

The γ at 298.15 K produced a vibrating surface energy unlike the optimized states at 288.15 and 308.15 K (Fig. 19, Table 10). The 298.15 K induces a transition state as the increasing GO concentration creates stronger edges and dipoles with nonlinear interacting activities. The H_2O monomers cement the GO in GO-H_2O-H_2O-GO, with cohesive forces between the newly oriented H_2O dipoles (Fig. 17). On increasing GO concentration, the dipoles detach and develop interfaces of functional edges and H_2O of smaller size, lowering the γ.

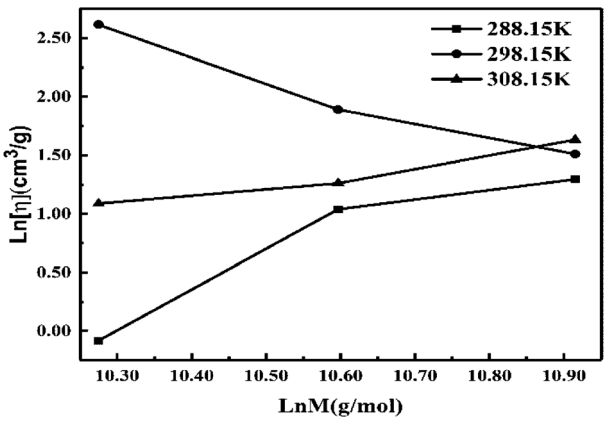

Fig. 18 $\ln[\eta]$ *vs.* $\ln M$ for M–H constants of aq-PVP.

Table 9 $\ln[\eta]$ *vs.* $\ln M$ of (Fig. 18)

T (K)	Intercept, k ($cm^3\ g^{-1}$)	Slope, a ($cm^3\ mol\ g^{-2}$)
288.15	−22.066	2.1534
298.15	20.296	−1.7264
308.15	−7.6427	0.8465

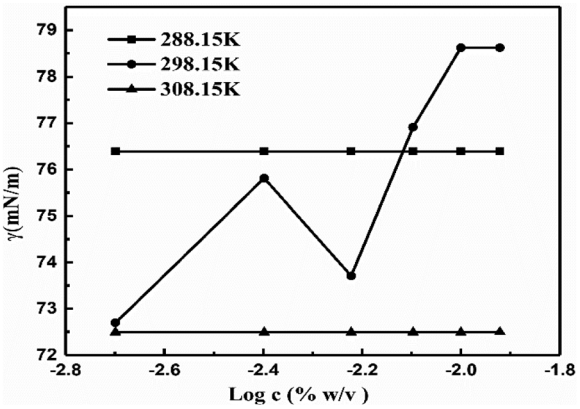

Fig. 19 The γ *vs.* log c for the surface excess concentration and surface area of aq-GO.

Table 10 γ *vs.* log c (Fig. 19)

Regression constants		
T (K)	Intercept ($mN\ m^{-1}$)	Slope ($mN\ cm^3\ m^{-1}\ g^{-1}$)
288.15	76.42	0.03
298.15	127.91	38.42
308.15	72.52	0.02

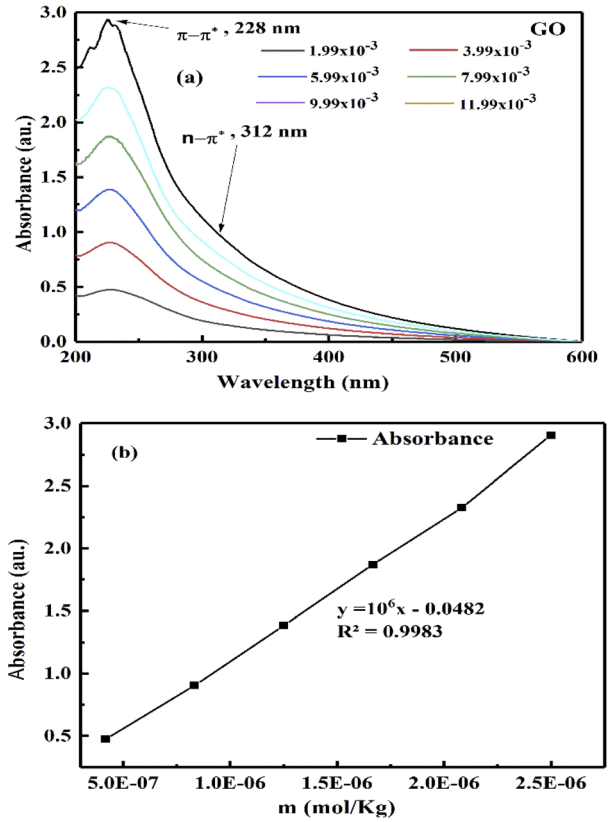

Fig. 20 (a and b) UV/vis absorbance *vs.* GO molality.

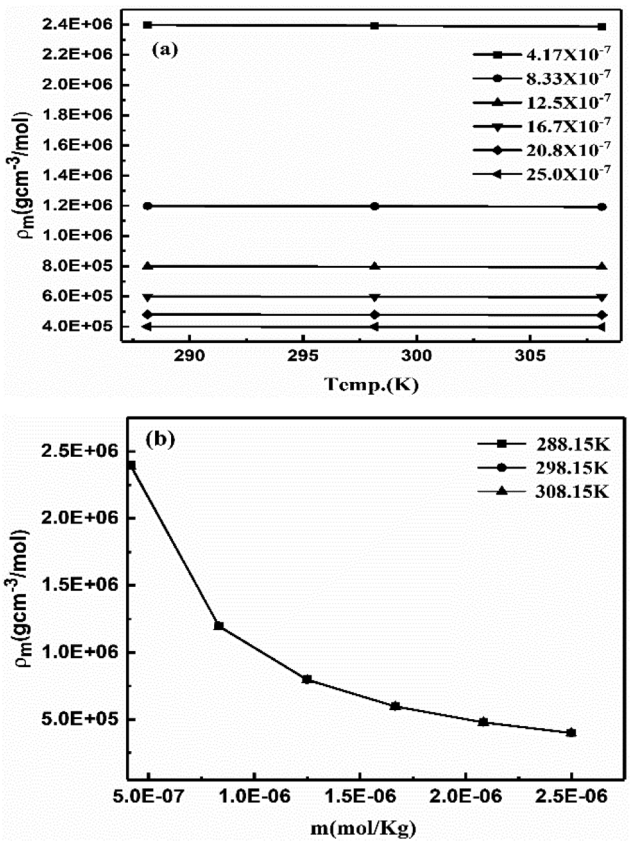

Fig. 21 Molar density *vs.* (a) temperature and (b) molality of aq-GO.

The intercept and slope values for log η *vs.* $1/c$ decrease on decreasing GO concentration due to the stronger activity (Fig. 13, Table 3). However, on decreasing the GO concentration, the slope values decreased due to a mild effect on the surface energy.

The rising temperature increased the V^0_{GO} on expansion of the core hydration sphere *via* interactions of the edges and dipoles *vs.* secondary interactions of the functional edges and electrostatic dipoles.

$$\text{Expansion coefficient, } V^0_{GO,T} = \frac{1}{V}\left[\frac{V_{GO}}{\partial T}\right]_{C,pH} \quad (3.0)$$

The V^0_{GO} infers an infinitesimal change with the secondary activities with a minor shift in activity with 10^{-7} order of isentropic compressibility. The different V^0_{GO} values with the same GO concentrations at different temperatures, show the temperature sensitivity of the functional edges and electrostatic dipoles. The V_ϕ is calculated from the density and M_v with their regression values ($V_\phi = 44\,655 + 12.191T$), closely agreeing with the experimental values. The V^0_{GO} is theoretically calculated using the values of the regression constants at 283.15 and 313.15 K which have the same order as experimental results (Fig. 16 and Table 5).

For 0.002–0.012 g%, there is no abrupt shift in V^0_{GO} as GO had polarized sheets with negligible changes on increasing concentration and temperature, as supported by the Raman spectra (Fig. 8). The polarized GO photodegraded the dyes efficiently and could be doped with TMI. On increasing temperature, the hydration sphere oscillates as the GO volume expands, avoiding the undesired structural defects of GO. The viscosity *vs.* GO concentration closely agrees with the literature values (Fig. 17b).[35] The ions of NaCl are reoriented by the GO charge distribution with the respective charged centre (Fig. 7). ESI Fig. 1.2a and b† infer the PCR at 298.15 K as no amount of energy induces a transition, and the GO-FE ≈ ED-H_2O uniformly responds to increasing GO moles. The viscosity and surface tension both infer the localised activities with a nonlinear trend on increasing GO concentration with a moderate shift within GO-H_2O. The interactions of the functional edges and electrostatic dipoles tune the alignment, unlike spherical aq-Na^+ and aq-Cl^- in bulk with a residual force. The values of shear stress from 25 °C and 35 °C have a gap the same as literature values from 25 °C to 65 °C at 10 °C intervals.[44] The values on increasing temperature reduce the gap negligibly in the reported values (Fig. 17a and ESI, Table 3.1†).

The slopes infer activities that are almost the same from 298.15 to 308.15 K, due to polarity. Hence PCR under sunlight is temperature independent. The higher GO concentration engages almost all the H_2O dipoles, so a further increase in GO concentration fades out as stronger GO–GO interactions are created. The log η_m *vs.* $1/m$ allows the calculation of E_a from the slope, and we can see the log η_m value decreases with increasing

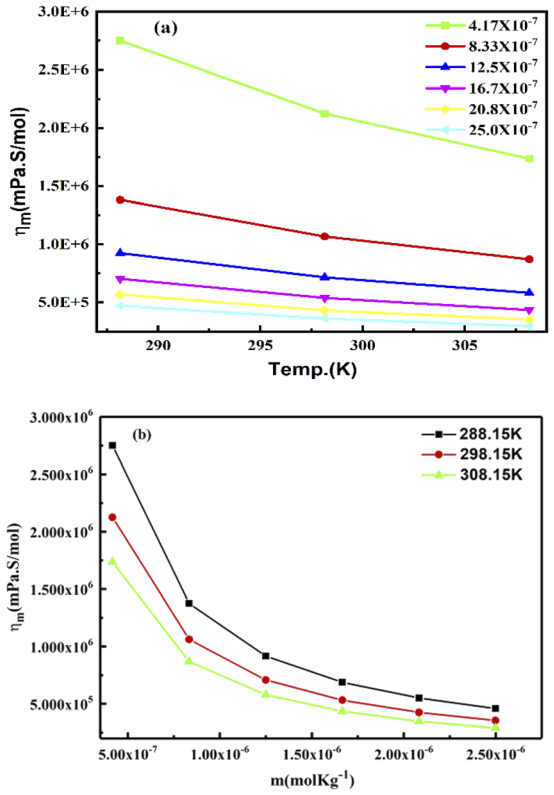

Fig. 22 (a) Molar viscosity *vs.* temperature and (b) molar viscosity *vs.* molality of aq-GO.

GO moles (Fig. 14, Table 4). The γ_m *vs.* log m allows the determination of surface area from the slope value (Fig. 15, Table 6). The $[\eta]$ infers interaction of the edges and dipoles of monodisperse GO during the redox cycles (Fig. 17).

The k and a determine @GO interacting activities of edges and electrostatic dipoles. The $\log[\sigma]$ *vs.* cohad forces align the GO, so its wavefunction effects laminar flow causing a velocity gradient that influences ψ_{e^-} ψ_{h^+} or ψ_{h^+} $\psi_O^{\delta--}$ and $(\psi_{h^+}$ $\psi_O^{\delta--}) - \psi_h^+$ through the partitioning of their energies with a maximum probability. The maximum probability could develop a steady state coordinating each hole with an intrinsic friccohesity in place of $[\eta]$. The monodispersed GO sheets had determined viscosity for M_v from the UV/vis, that connect functionality with molar activity (Fig. 4). The increasing GO moles with maximum number of functional edges capture maximum photons with their 1st order absorbing ability. The absorbance *vs.* molality of GO generated is given by eqn (3.1)

$$\mathrm{Abs}_{GO} = -0.0482 + 1 \times 10^6 x. \quad (3.1)$$

The 1×10^6 slope infers stronger photon absorption with hole generating ability to overcome the quantum energy barrier (QEB), while extrapolation to $C_{GO} \rightarrow 0$ concentration gives lower Abs than the solvent. TMI-GO with a single $\hbar\nu$ generates phonons behaving as upconversion nanoparticles (UCNP).[45]

Aq-GO absorbs UV light linearly at $\lambda_{max} = 228$ nm within 200–600 nm on increasing concentration (Fig. 20b). The ^{13}C NMR produced a straight line along the x-axis with no sharp peak due to a GO single lattice, as the external magnetic field did not influence the functional groups bonded with the C–C skeleton of GO.[46] No effect of an external magnetic field on the electronic cloud of the C atom in a hexagonal GO sheet, shows that shielding in GO and TMI-GO could allow use as a sensor for a catalysis process in high magnetic fields. For a lower concentration, the higher gap infers the availability of functional edges as temperature disrupts the alignment of GO (Fig. 21a). The molar properties are sensitive to % concentration values, so a molar scale would predict accurate concentration effects (Table 6). The ρ_m decreased and V_{ϕ_m} increased upon increasing GO moles as the GO sheet expands with the stronger interactions, while the stronger interactions decreased the V_{ϕ_m} and ρ_m with weaker alignment (Fig. 21). The GO-H_2O interactions sandwich the H_2O between the GO sheets which expands from both sides to attract the H_2O (Fig. 17).

Lower GO moles have stronger electrostatic interactions restricting alignment, so the molar activities account for the contribution of each GO constituent. The aq-GO developed single walled carbon nanoparticles on its surface as a slippery sheet. The H_2O molecules adhere to the GO sheets despite acquiring an energy with a lower γ with a higher ϕ_m. On increasing the GO moles, the ϕ_m increased to 16.7×10^{-7} and then became constant at 298.15 K while at 308.15 and 288.15 K, the ϕ_m decreased to 12.5×10^{-7} and then increased (ESI, Fig. 1.8a and b†). The η_m *vs.* m polynomial trends show decreasing ΔG values with increasing GO moles (Fig. 22b, ESI Fig. 1.9†). Considering dissolving GO moles, the constant ΔG is used irrespective of the η_m *vs.* m trend. The shift in η_m from lower to higher molality was adhered to in a 1 : 1 ratio affecting aq-GO fluid dynamics (eqn (3.2)).

$$\eta_m = \left(\frac{\partial \eta}{\partial m}\right)_{T,P,C} \quad (3.2)$$

Aq-GO is a Newtonian liquid, so the ΔG *vs.* m linear trend infers nanoclustering (ESI, Fig. 1.9a and b†). The polynomial η_m *vs.* m with lower GO mole interaction should have compensated for the ΔG *vs.* m with the water–GO interaction, unlike with GO–GO alignment, it did compensate at higher GO moles. The HB and GO–GO interactions might have utilised the ΔG on increasing molality. The HB disruption forms H_2O–GO–H_2O = GO$(H_2O)_n$ at lower concentrations,

$$\Delta G_{\text{HB disruption in aq-GO}} = \Delta G_{\text{HB disruption in GO–GO}}$$

The oscillations saturate between 298.15 to 308.15 K, the R_m needs an almost equal ΔE_{am} at 298.15 and 308.15 K,

$$\psi_{298.15K} = \psi_{308.15K} = \frac{P^2}{2m} - \frac{q^+q^-}{4\pi\varepsilon_o r^2}. \quad (3.3)$$

The ΔG values decrease on increasing GO moles reducing QEB, at $3T$ (ESI, Fig. 1.9a and b†). The GO sheets are fragmented at the freezing and boiling points, and under electrophoresis, so the M_v could not be measured. For MALDI-TOF, the GO was mixed with matrixes of 20 to 60 kDa (kilodalton) to fragment it,

but the covalent C–C skeleton was not disrupted. A MALDI-TOF intensity from −500 to 1500 (a.u.) *vs.* 40 000 to 54 000 g mol^{-1}, could not distinguish a decisive distribution and so failed to produce a mol. wt. (ESI, Fig. 3.6†). LC-MS also failed as unfragmented GO did not respond to a quadrupolar magnet, the GO sheet reoriented, so a survismeter method was used to determine M_v. The wavefunction increases on rising temperature, but at $m \rightarrow 0$, the sheets are separated. The wavefunction infers the H_2O acts as a sheath between the GO sheets. The electrostatic stabilisation of the H_2O as a barrier could not pass the oscillating motions from one GO sheet to another despite 2D spreading. These deviations in volume depict the lowest distance between the functional edges and electrostatic dipoles. The ions were activated but the $H^{\delta+}$ were covalently bonded with the H_2O, and it was difficult to disrupt the covalent bonds compared to counterbalancing the ions. The salts dissociated, where the $H^{\delta+}$ activated the GO for the redox cycle without acquiring much activation energy. The studies are prerequisites to explain Φ. The coefficient $[\eta]/[V_0]_{m\rightarrow 0}$ infers alignment of the functional edges and electrostatic dipoles to functionalize the GO with TMI and to photodegrade the dyes depending on concentration. The aq-GO sheet with functional edges and electrostatic dipoles interacting, has a higher relaxation time within a capillary unlike the pendant drop method that has free area available for cohad forces: so no relaxation time is required for the pendant drop number. The GO develops the 1 : 1 redox cycles, despite being restricted to the original state of C atoms in GO, and its size multiplying the holes. So a NaCl → Na^+ + Cl (1 : 1) electrolyte was chosen *vis-á-vis* GO laminar sheet arrays.

A basic difference in GO and NaCl is dislocation of the spatial position to develop unhindered interactions between nanohydration spheres (NHS–NHS) with opposite charge. The GO has the lowest E_a so the photon did a more PCR, unlike for aq-NaCl that acquired energy from the H_2O. The NaCl dissociates into Na^+ and Cl^- as fully independent positive and negative charges, unlike the GO holes that generate the redox cycles. The NaCl disrupts the HB unlike GO that splits the water ($H_2O \rightarrow H_2 + O_2$). The dissociating and H_2O interacting peculiarities *vis-á-vis* activities of GO to split H_2O, clearly distinguish GO and NaCl. The study of MPs of aq-NaCl and aq-GO as a secondary bond *i.e.* HB reoriented by γ_{Na^+} and γ_{Cl^-} with stronger interactions at a nm distance, was conducted. It caused a downward pull only in the *z*-dimension where a monolayer of H_2O exists but the bulk solution did not have residual electrostatic dipoles: NaCl $\rightleftharpoons$ $Na^+ + Cl^-$, $\gamma_{\pm} = \gamma_{Na^+} + \gamma_{Cl^-}$ and $Na^+ = Cl^-$, $\gamma_{\pm} = \gamma^2$. So, FE $\rightleftharpoons$ $h^+ + e^-$, $\gamma_{\pm} = \gamma_{h^+} + \gamma_{e^-}$ and $h^+ = e^-$ $\gamma_{\pm} = \gamma^2$ where γ is the activity coefficient. The Gt and GO both have strong alternative covalent bonds and mutual hybridization occurs. The same trend is obtained with the NaCl and GO, however on increasing concentration and temperature, the viscosity decreased (ESI, Table 3.1 and 4.0†). The negative value of the slope shows the weaker cohesive forces (ESI, Table 3.8†). The 288.15 K distinguishes the salt–water interaction unlike at 298.15 and 308.15 K (ESI, Fig. 2.4a†). At 298.15 K, all the apparent molar volumes are distinguished at lower concentration, but at a higher concentration the temperature could not be detected due to stronger salt–salt saturated interactions. No ionic charge is available that could oscillate on gaining kinetic energy. The lower NaCl concentration shows a maximum oscillation at lower temperature but on increasing its concentration the temperature shows no significance. This action mechanism defines that the NaCl concentration is temperature sensitive as the residual charges at 288.15 K are comparatively more sensitive, unlike at 298.15 and 308.15 K (ESI, Fig. 2.4b†).

aq-GO doped with TMI *via* photonic interaction

The functional edges of GO efficiently develop negative and positive holes to substantiate the intensified redox cycles for photocatalysis. Transitional metal ions have variable valence electrons, and the sole objective for using these metal ions was to sandwich their variable electrons between the functional edges of GO, supporting HOMO to LUMO transitions. In regard to current interest in recycling wastewater, our studies have been designed to combine the advantages of the variable electrons of TMI and the functional groups of GO. The variable redox cycles generated out of the functional edges boosted by the functional groups of the GO, have tunable fluid dynamics – an excellent model of laminar or Newtonian fluid out of the symmetric GO sheet. Such TMI-GO driven nanothin films could act as the photonic sensors, be used in touch screen technology, heat dissipating sensors and similar. Therefore, the metals ions-doped GO can generate efficient robust redox cycles.

The GO was doped with Cr^{3+}, Fe^{2+}, Mn^{2+} or Ni^{2+}, forming TMI-GO in aq-chloride salt in sunlight within ∼30–90 min. The TMI-GO with unevenly distributed holes created a different pressure on surfaces with a different kinetic energy (Fig. 23, eqn (3.4)),

$$\frac{P^2}{2m} > \frac{q^+q^-}{4\pi\varepsilon_o r} \tag{3.4}$$

The resonating holes develop a wavefunction in the same phase as the ions, with ψ_{cat} and ψ_{an} aligning from ψ_{h^+} and ψ_{e^-}, respectively. The charge countering activities interact with the H_2O dipoles to bond them in place, the cohesive forces are exchanged mutually as,

$$\psi_{cat} \gtrless \times \psi_{e^-} = \int_0^n \psi_{cat} \ominus \int_0^n \psi_{e^-} \oplus = \oiint \psi^2 > \mathrm{QEB} \tag{3.5}$$

Eqn (3.5) predicts GO as a doped sheet with negative and positive holes to oxidise the Cl^- as $2Cl^- + 2h^+ = Cl_2$. The ions have been reduced to metal GO frameworks within the GO spatial lattice (Fig. 23a–d).

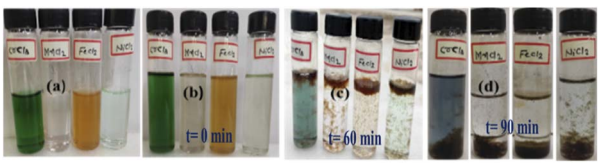

Fig. 23 (a) Aq-salt, and absorption of aq-salts by GO at time (b) 0, (c) 60, and (d) 90 min.

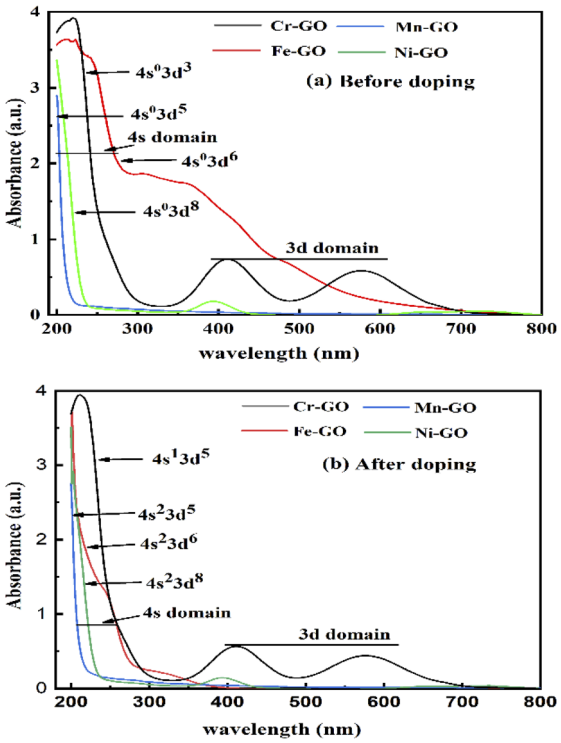

Fig. 24 UV/vis for TMI-GO (a) before and (b) after, doping.

In UV/vis, Cr-GO, Mn-GO, Fe-GO, and Ni-GO utilizing 105.1, 100, 109.4 and 100% quantum absorption yield (Φ_{QA}), respectively (Fig. 24 and ESI Table 5.1†). The $Cr^{3+}(4s^03d^3)$ receives $3e^-$ holes from GO for quantum absorption: $1e^-$ hole in the 3d orbital and $2e^-$ holes in the 4s orbital, generating two UV/vis peaks, respectively (Fig. 24a and b). The $Mn^{2+}(4s^03d^5)$, $Fe^{2+}(4s^03d^6)$ and $Ni^{2+}(4s^03d^8)$ receive the $2e^-$ holes in the 4s orbital that generate peaks at $\lambda = \sim 200$ nm. The higher potential energy of paired electrons compared to unpaired, neutralises the oscillations of unpaired electrons generating weak oscillations as $\psi_{\text{paired electrons}} \leftrightarrow \psi_{\text{unpaired electrons}}$.

The salts form cages around the cations forming NHS and aligning the H_2O dipoles. The oxidation state *vs.* NHS reduce the cation where a cage acts as the electronic barrier (H_2O-TMI-H_2O). UV/vis at 228 nm produces >0.7 abs with the HOMO → LUMO state retaining 70% of the UV light. From 200 to 800 nm, the Mn^{2+} with abs = 0 aligned with an enhanced mechanism (Fig. 24). The Mn-GO could be a promote surface enhanced Raman sensor, unlike Ag-pyridine. Fe-GO and Ni-GO have fluctuating UV/vis abs due to a few paired electron spins. The Cr ($3d^3$) has two empty d orbitals to oscillate, and Mn-GO aligns the GO sheet at 90° with no oscillatory disruption; Mn ($3d_5$), Fe ($3d^6$) and Ni ($3d^8$) oscillate symmetrically. TMI-GO could be developed as an antibacterial or antifungal with antioxidant activities.[38] The Mn^{2+} ($4s^03d^5$) and Fe^{2+} ($4s^03d^6$) have a difference of $1e^-$ having 109.43 and 100% Φ_{QA}, respectively. The Φ_{QA} depends on the number of photons absorbed and emitted during PCR (ESI, Table 5.1†).

Table 11 ICP-OES analysis of TMI-GO

Analyte quantity	Corresponding intensity (g)	Prepared concentration (mg L^{-1})
Cr 267.716	6416.2	1.584
Mn 257.610	833 906.2	30.57
Fe 238.204	16 539.7	3.30
Ni 231.604	34 206.2	27.53

Using ICP-OES we detected the different amounts of TMI in the TMI-GO templates (Table 11). The TMI was washed before ICP detection, an equal stochiometric ratio of all metal ions was taken. The transition metal ions were adequately doped onto the GO sheets where their valency and nuclear sizes – the number of functional edges of the exfoliated GO sheets – were proven to be the prime consideration. The TMI-GO templates enhance the photocatalysis of methylene blue compared to GO alone, and the ICP-OES results also confirmed the substantial chemical binding of the transition metal ions with those of the electron clouds of the functional edges of the GO.

Stronger bonding of TMI within TMI-GO reduces the IR peak as C atoms affect the oxide atom creating strong metal oxide stretches (ESI Fig. 4.2†). The GO attached to TMI stretched robustly symmetrically. ESI Fig. 4.2† infers photonic interactions with the GO reducing it to rGO; some functional groups are missing when compared to GO, and new ones appear, induced by the TMI (Fig. 6). A lower intensity of TMI-GO infers its monodispersion of oscillations. The functional edges of TMI-GO hold the H_2O, and binding of TMI is explored.

The XPS spectra show the chemical composition and oxidation states of TMI binding with GO at certain binding energies of the inner electron. Fig. 25a shows the binding energy of Mn-GO and Ni-GO where the C ($1s^22s^12p_x^12p_y^12p_z^1$) atom of GO binds with the O atoms of –COOH, –OH, –O– and >CO, differing in their binding energies. The XPS of C 1s of Mn-GO and Ni-GO at 284, 284.8, and 287.1 eV, infer the activities of the sp^2 C atom, –C–C and –COOH, respectively, due to electron clouds of the adjoining atoms (Fig. 25b). XPS spectra of O 1s of Mn–GO and Ni–GO at 530.87, 531.7, and 533.48 eV for C–OH, C–O–C and C=O respectively depict their binding stabilities (Fig. 25c). The binding of C atoms with oxygen creates a gradient among C atoms of GO with a spontaneity to make GO receptive to respond to the TMI-GO. The binding energies are 853.2 and 870.6 eV for Ni $2p_{3/2}$ and Ni $2p_{1/2}$, respectively, along with the similar values of C 1s for C and O 1s for the O atoms (Fig. 25a–c). Similarly, the binding energies, are 641.18 and 653.33 eV for Mn $2p_{3/2}$ and Mn $2p_{1/2}$, respectively.[4] The large energy difference between the Mn 2p and Ni 2p is due to the paired and unpaired electrons. The intensity of the –C=O and –C–O reduced compared to the C–C, as GO underwent oxidation with different electronic clouds. Excellent hybridization occurs between the C and O atoms. The contribution of energy from the O 1s electron in the C skeleton, with the 1 s electron of the metal, is strong with a nucleus forming the skeleton of the GO sheets. The sharp peak of GO disappeared on binding of the TMI. The $\psi_{TMI} = \psi_{FE}$ oscillations of half-filled 3d

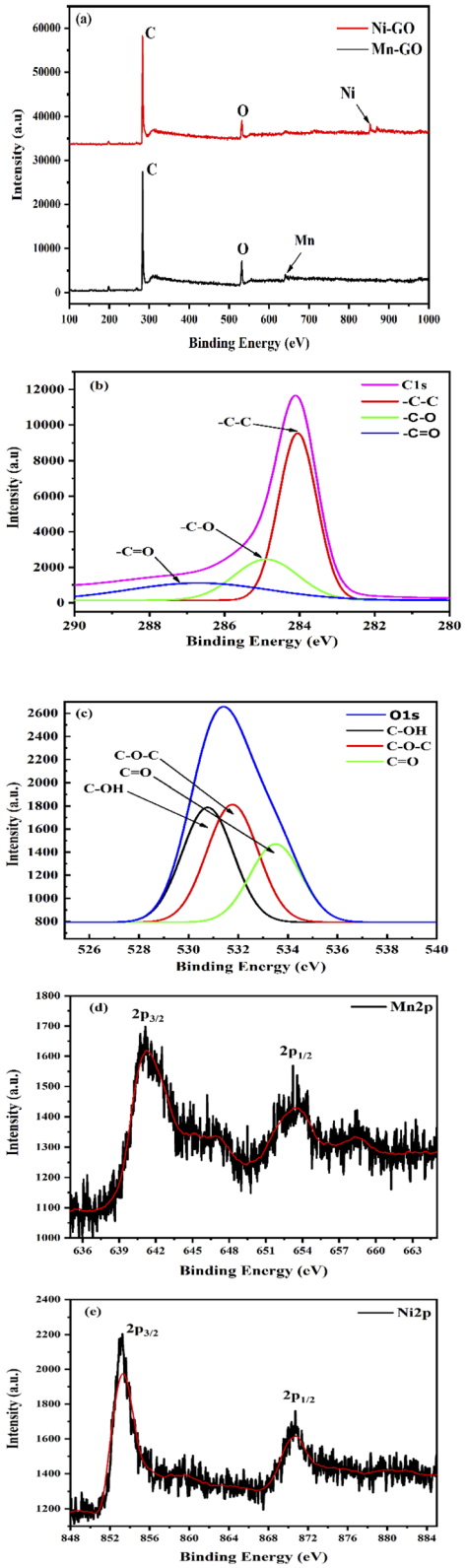

Fig. 25 (a) XPS of Mn-GO and Ni-GO survey spectra, (b) C 1s, (c) O 1s, (d) Ni 2p, and (e) Mn 2p.

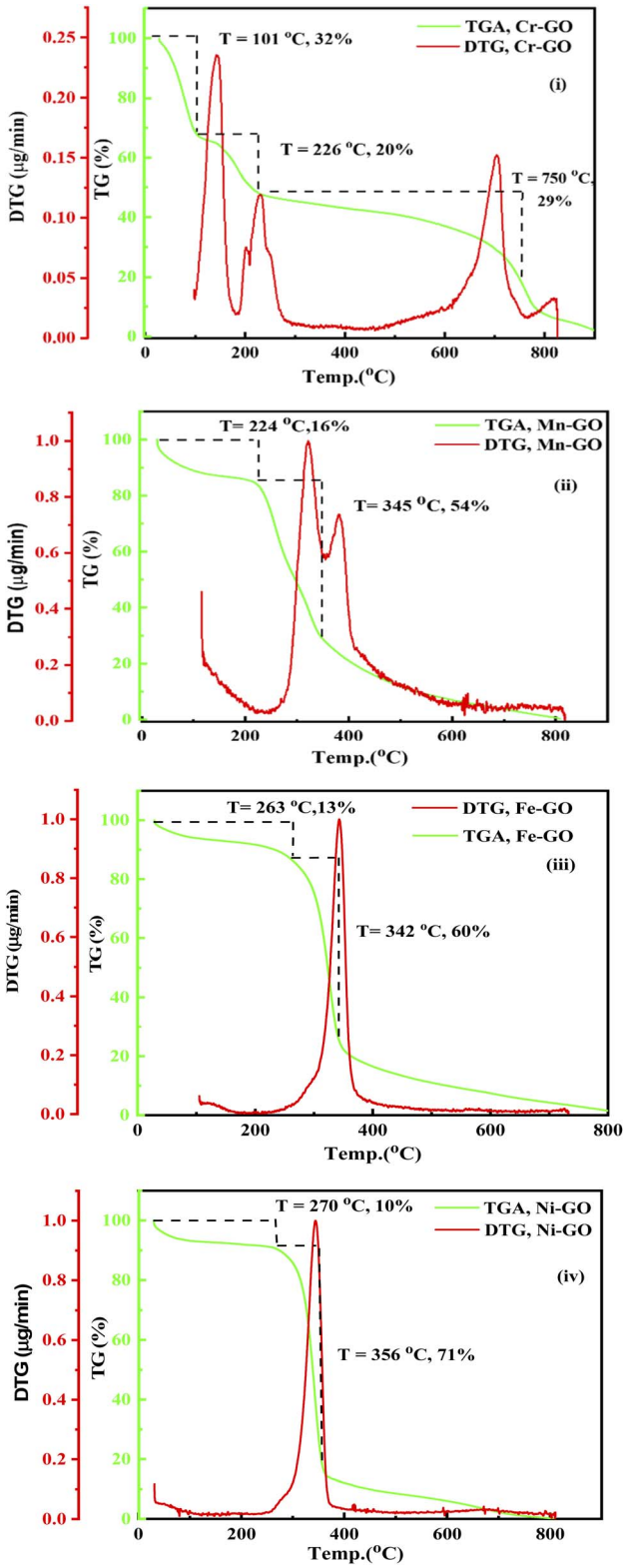

Fig. 26 TGA and DTG: (i) Cr-GO, (ii) Mn-GO, (iii) Fe-GO, (iv) Ni-GO.

e^- of Mn ($4s^2 3d^5$) approached the conduction band of the 4p orbital and conduction band of the GO. The valence band of TMI could approach the conduction band of GO. The unengaged lattices of the 2D GO sheets provided XRD with maximum intensity. Upon doping, the electronic clouds of the functional edges were engaged by the TMI; so the sharp peak of GO at $2\theta = 8.85°$ was lost (ESI Fig. 4.3†).

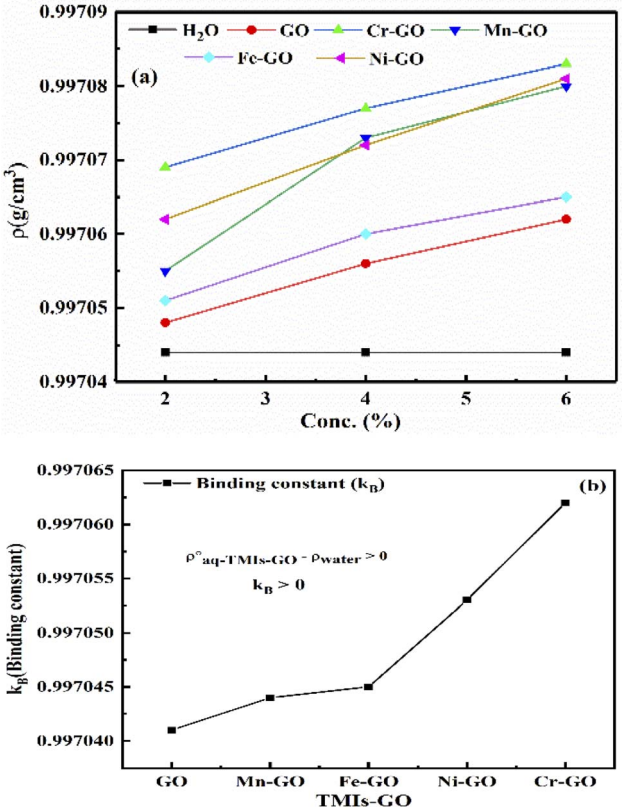

Fig. 27 (a) Density *vs.* concentration, (b) binding constant between aq-GO and TMI.

FE were not blocked by ions; instead they homogenise when they do not acquire sufficient energy to reach the oxidation potential of M^{n+}. TMI-GO enhanced the water absorbing ability at low temperature. The GO could absorb 18% water at 136 °C and Cr-GO absorbs ~32% at 101 °C (Fig. 3 and Fig. 26(i)). The TMI *vs.* C in the GO network develops large nuclear charge differences at a higher temperature. The C atoms in GO have a single lattice with a corresponding peak appearing in the TGA spectra (Fig. 26(i)). On heating, the e^- gets excited and then returns to the ground state, so the single lattice has the same oscillations producing a single sharp peak in the TGA. TMI in TMI-GO is attached to carbon of the GO, so the oscillations of the sheet are changed. The heat capacities of different patches with different e^- produce different lines in the TGA (Fig. 26(i–iv)). New lattices are developed with new oscillation patterns with different wt losses, where no H_2O is present at 224 °C except crystalline H_2O. Two peaks with five unpaired e^- oscillate, which cannot occur in a lattice so the nuclei are responsible for the peaks (Fig. 26ii). The e^- of Cr-GO oscillates at a lower energy with a wt loss at lower temperature, unlike Mn-GO at 224 °C (Fig. 26(ii)). A single lattice is formed where a paired e^- neutralizes the unpaired e^-; together the e^- provide a similar lattice on gaining equal heat with a single peak at 356 °C. Fig. 3 and 26(iii), depict Fe^{2+} doping with functional edges and show the enhanced activity of TMI-GO on losing a least wt until 800 °C, due to increased stability of the TMI-GO (Fig. 26).

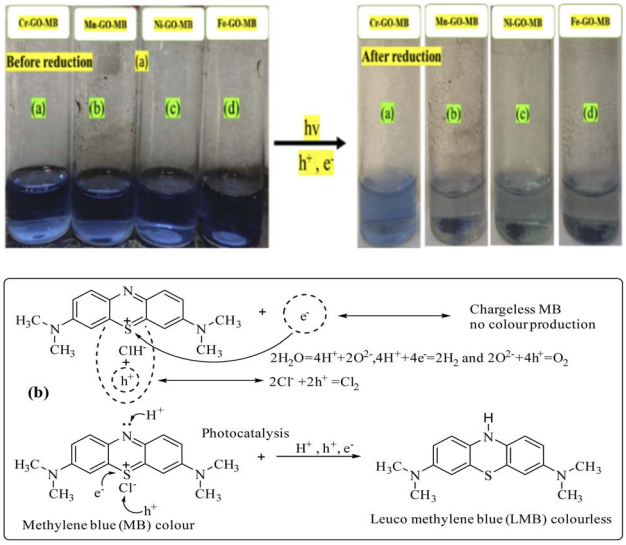

Fig. 28 (a) Reduction of MB by TMI-GO in sunlight and (b) the proposed mechanism.

Fig. 27(a and b) provide the binding constant (k_B) of TMI-GO as calculated by extrapolation of density *vs.* concentration. The lower GO densities with increasing concentration, compared to TMI-GO, infer the accommodation of TMI within a sheet without disrupting the GO geometry. With increasing concentration, Mn-GO shows a slightly different trend, due to a half-filled d-orbital with ultrasensitive GO, where the smallest bandgap generates conductivity: their 3d electrons bind with GO for functionality. The Mn-GO acts as a more robust photocatalyst than the other TMI. The k_b values are given in Table 12.

MB has a symmetric structure with continuous π-conjugation along with hydrophobic methyl groups at the terminal sites of the benzene rings. MB responds strongly to photons – unlike brilliant blue red (BBR) and brilliant blue green (BBG) – due to its quaternary nitrogen atom which is reduced (Fig. 28). The MB as a whole can also be reoriented under SL, and responds to the holes generated by GO at the closest permittivity and lowering of the QEB. The chloride ion attached to the quaternary nitrogen vibrates the secondary bond and detaches, resulting in lower activation energy to engage the positive holes (Fig. 29). MB fits in the intersheet arrangement of GO or TMI-GO, however, PCRs replacing MB using BBR and BBG are being pursued.

GO alone takes longer to catalyse PCR of MB than TMI-GO (Fig. 30).[4]

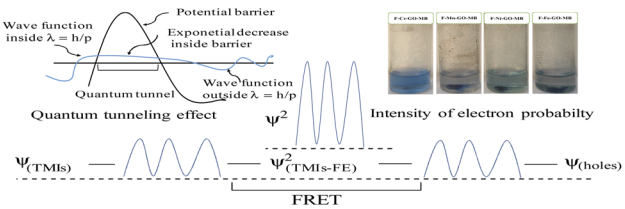

Fig. 29 Quantum tunnelling effect during reduction, which produces wavefunctions.

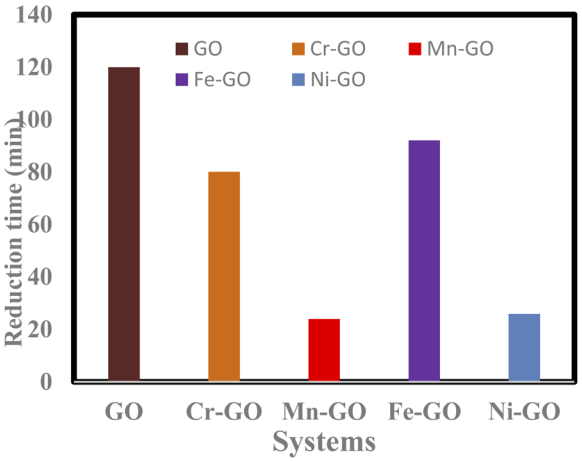

Fig. 30 Time taken for GO and TMI-GO to reduce MB.

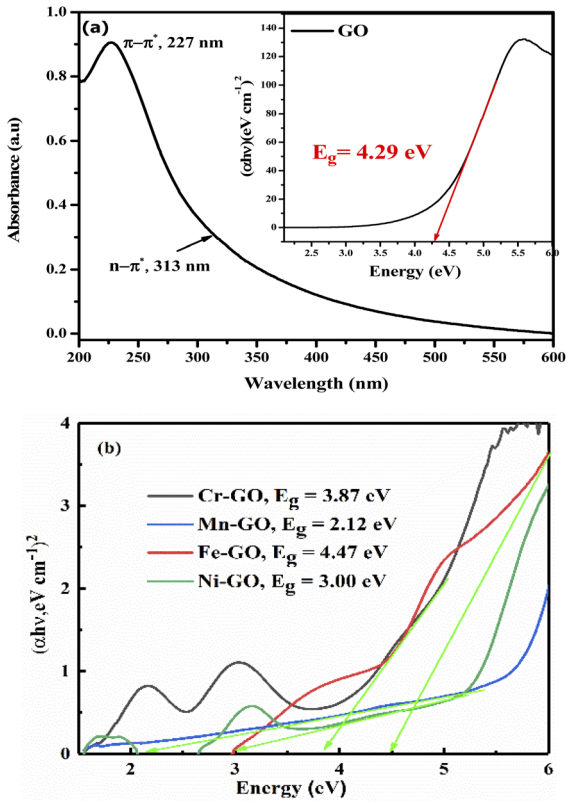

Fig. 31 (a) Bandgap energy from the Tauc plot of: (a) aq-GO and (b) the TMI-GO samples.

$$\text{Time shift} = t_{(\text{TMI-GO})} - t_{(\text{TMI-GO-MB})} \tag{3.6}$$

The bandgaps of GO and TMI-GO were determined from the Tauc plot as

$$\text{Bandgap energy } (E_g) = \frac{hc}{\lambda},\ \alpha = \frac{\text{Absorbance (UV)}}{\text{Thickness } (d)} \text{ and } (\alpha h\nu) = B(h\nu - E_g)^n \tag{3.7}$$

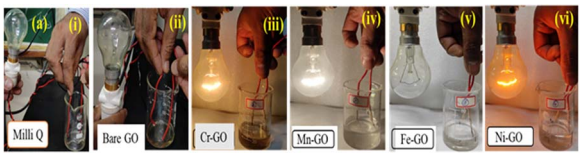

Fig. 32 Conductivity of: (i) pure water; (ii) aq-GO; (iii) Cr-GO; (iv) Mn-GO; (v) Fe-GO; and (vi) Ni-GO.

where α is the absorption coefficient, E_g the optical bandgap, B the band tailing parameter, $\hbar\nu$ is photon energy, and $n = \frac{1}{2}$ for the direct bandgap. The E_g is calculated by extrapolating a straight-line from the curve between $(\alpha\hbar\nu)^2$ *vs.* $\hbar\nu$ when α is equal to zero. The bandgap for GO, Cr-GO, Mn-GO, Fe-GO, and Ni-GO are 4.29, 3.87, 2.12, 4.47 and 3.00 eV, respectively (Fig. 31). Mn-GO conducts electricity (Fig. 32): as the interface between Mn and GO increases, absorption occurs due to the HOMO → LUMO transition. The Mn-GO quantum absorption infers nanocluster formation at 2.12 eV E_g (Fig. 31). Hence the choice of TMI affects the resultant nanocluster bandgap size (Table 12).

The smooth Mn-GO surface quenched any undesired surface charges, and is a heat, acid–base and chemical resistant structure. 70% Φ of GO is attained yet the aq-GO does not conduct electricity due to the larger bandgap, despite the holes with a confinement of E_g = 4.29 eV. The lower TMI-GO amount reduces a large amount of dye due to the aligned holes with a shorter bandgap that generate surface plasmonic resonance (Fig. 31).

neither aq-GO or Millipore water can light a bulb upon connection with 220 V at RT. However, TMI-GO allows electricity flow – the Mn-GO catalyses PCR of MB in 62 min due to stable poles, but Fe-GO has large E_g (4.47 eV). aq-GO as a sensor can determine conductivity and concentration variations.

The adsorption activity of MB by TMI-GO is calculated as

$$E_{abs} = \frac{hc}{\lambda_{abs}},\quad E_{em} = \frac{hc}{\lambda_{em}},\quad n_a = \frac{E_a}{h},\quad n_e = \frac{E_e}{h},\quad \Phi = \frac{n_e}{n_a} \tag{3.8}$$

where E_{abs} is absorbed energy, E_{em} is emitted energy, n_a is the number of photons absorbed, n_e is the number of photons emitted, ($\lambda_{abs}$is the absorbed wavelength, λ_{em} is the emitted wavelength and Φ is quantum yield.

$$\frac{C_0 - C_t}{C_0} \times 100 \text{ and } \frac{20 - 2.867}{20} \times 100 = 85.67\% \tag{3.9}$$

C_0 is the initial MB concentration at time $t = 0$, and C_t is amount of reduced MB at t min. MB reduction of 98.7, 98, and 98.4% > GO by Mn-GO, Fe-GO and Ni-GO was found, respectively. The λ_{abs} is 663, 661, 665, 664 and the λ_{em} is 668, 665, 668 and 675 for (Cr-GO)-MB, (Mn-GO)-MB, (Fe-GO)-MB and (Ni-GO)-MB, respectively (Fig. 33). The Φ for MB reduction by (Cr-GO) is given by eqn (4.0)

$$\lambda_{abs} = 663 \text{ nm and } \lambda_{em} = 668 \text{ nm},$$

$$E_{abs} = 2.9982 \times 10^{-19} \text{ J},\ E_{em} = 2.9757 \times 10^{-19} \text{ J}$$

Table 12 Rate of PCR and bandgap energy of TMI-GO with binding constant

TMI-GO	Doping time (min) TMI-GO	Reducing time (min) GO-TMI : MB	Time shift	E_g (eV)	k_b of TMI-GO (10^{-5})
Cr-GO	150	70	80	3.87	2.1
Mn-GO	62	38	24	2.12	1.4
Fe-GO	118	26	92	4.47	0.33
Ni-GO	78	52	26	3.00	1.63

$$n_a = \frac{2.9982 \times 10^{-19}\ \text{J}}{6.626 \times 10^{-34}} = 4.52488 \times 10^{14}\ \text{s}^{-1},$$
$$(n_{em}) = \frac{2.9757 \times 10^{-19}\ \text{J}}{6.626 \times 10^{-34}} = 4.49102 \times 10^{14}\ \text{s}^{-1} \quad (4.0)$$
$$\Phi_{(\text{Cr-GO})\text{-MB}} = \frac{n_e}{n_a} = \frac{4.49102 \times 10^{14}\ \text{s}^{-1}}{4.52488 \times 10^{14}\ \text{s}^{-1}} \times 100 = 99.25\%$$

The Φ for (Mn-GO)-MB, (Fe-GO)-MB and (Ni-GO)-MB are 99.40, 99.55 and 98.37%, respectively. The Φ for MB reduction is 99.55 (Fe-GO) > 99.40% (Mn-GO) > 99.25 (Cr-GO) > 98.37% (Ni-GO) where the Fe-GO and Mn-GO have maximum Φ with E_a. TMI-GO reduced 99.14% MB compared to 88% by GO alone (Table 8).

aq-GO can photodegrade sugar, caffeine and the phytochemicals of tea with milk in 2 h, followed by H_2O splitting and the appearance of the black fine powder of CNPs (Fig. 34c): the GO on receiving a photon reduces the π-conjugation of caffeine

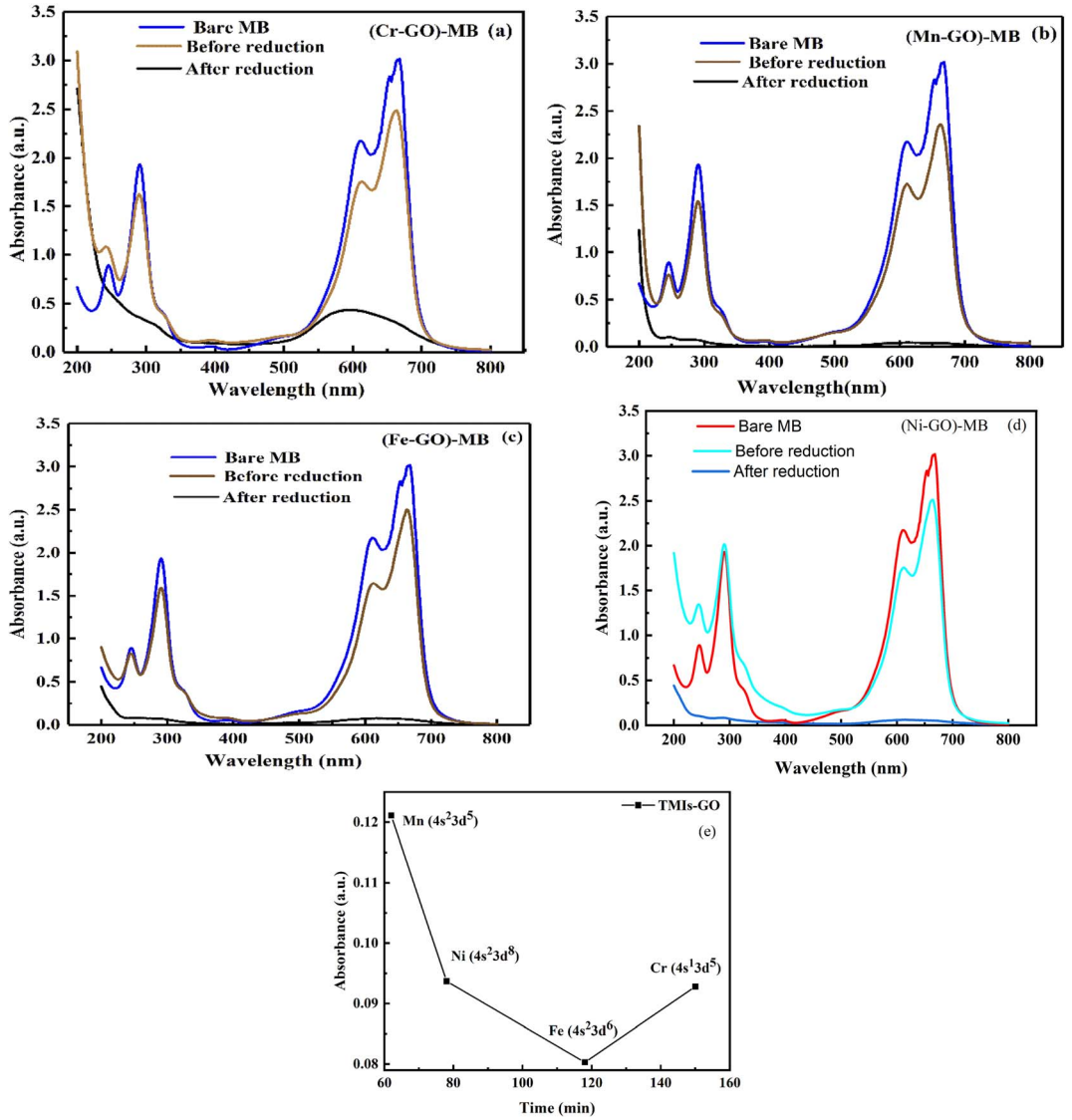

Fig. 33 UV/vis before and after MB reduction with: (a) Cr-GO, (b) Mn-GO, (c) Fe-GO, (d) Ni-GO and (e) absorbance *vs.* temperature for each TMI-GO-MB.

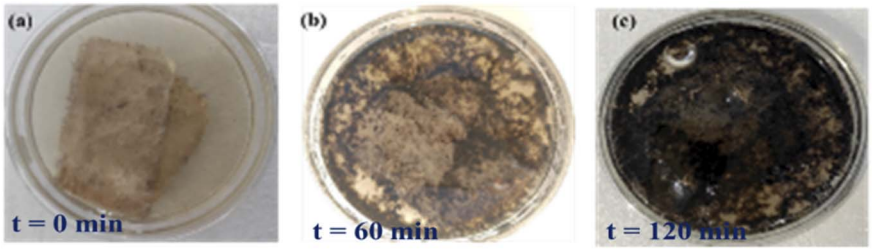

Fig. 34 Degradation of tea contents with aq-GO in sunlight.

($C_8H_{10}N_4O_2$). The sheets are aligned to store the energy received from solar radiation as photons. The caffeine and sucrose were both monodispersed on cotton to gain a high surface area for disposal, allowing collection of the purest CNPs. After 2 h under sunlight, the intense black CNPs were formed on the fabric and were collected without a filter. The CNPs could then be used for various chemical processes, with Mn-GO providing enhanced recovery of CNPs from the biomass of tea. Such a method could potentially even be used to dispose infectious medical biomass in place of incinerators (Fig. 34a–c).

Conclusions

The 48 134.19 g mol^{-1} of GO determined at 298.15 K is comparable to the value of M_v at 288.15 K and 308.15 K. Using M_v at these temperatures, we have calculated the molar properties to determine the molar activities of aq-GO. Molar properties determine molar activities with $a = \gamma_m$. The M_v provides calculated, apparent, and limiting molar volumes $(V^0_{GO})_{G\bar{O}0}$, enthalpy, entropy, viscosity, surface tension, friccohesity, fractional volume and isentropic compressibility. These values infer the integrity of GO sheets of 48 134.19 g mol^{-1} M_v: we studied the potential impact of 0.002–0.012 g% aq-GO undergoing aggregation, coalescence, nano-clustering and coagulation in a capillary flow. GO was then doped with Fe^{2+}, Mn^{2+}, Ni^{2+} or Cr^{3+} (TMI) under sunlight for ~30–90 min. TMI-GO can reduce MB and enhance PCR to 99.14% compared to 88% by GO alone. Each TMI reduces the GO bandgap and generates conductance, except for Fe-GO. The bandgap for GO, Cr-GO, Mn-GO, Fe-GO, and Ni-GO are 4.29, 3.87, 2.12, 4.47 and 3.00 eV, respectively. The metal-doped graphene framework was 1.58, 30.57, 3.30 and 27.53 mg L^{-1} for Cr-GO, Mn-GO, Fe-GO and Ni-GO, respectively, as analysed by ICP-OES. The $[\eta]$ values at 288.15 and 308.15 K have produced 46 886.03 and 42 845.25 g mol^{-1}, respectively; with an average $\bar{M}_v$ 45 955.16 g mol^{-1} which is 4.53% lower compared to 48 134.19 g mol^{-1} at 298.15. The calculation of the C atoms number of 4011, 688 hexagonal sheets, 222 π-conjugations, and 4011 FE is possible from the determined M_v. These are critical operators for photocatalysis and directly affect photon acceptance and hole generation. Thereby, such intrinsic data determination is not possible using only g%.

Appendix

Table 13 The secondary parameters of aq-GO at 288.15 K[a]

Conc. (g% w/v)	σ (10^{-2})	ϕ (10^{-3})	$K_{S\phi}$ (10^{-7})	V_ϕ (10^4)
0.002	1.500	2.83	4.65388	4.81778
0.004	1.508	5.13	4.65371	4.81773
0.006	1.514	6.66	4.65293	4.81772
0.008	1.535	12.50	4.65364	4.81766
0.010	1.550	16.30	4.65283	4.81762
0.012	1.439	13.40	4.65217	4.81759

[a] σ = friccohesity (scm^{-1}), ϕ = fractional volume (cm^3), $K_{S\phi}$ = isentropic compressibility (10^{-1} cm s^2), V_ϕ = apparent volume (cm^3).

Table 14 The secondary parameters of aq-GO at 298.15 K

Conc. (g% w/v)	σ (10^{-2})	ϕ (10^{-3})	$K_{S\phi}$ (10^{-7})	V_ϕ (10^4)
0.002	1.217	−2.42	4.47656	4.82765
0.004	1.173	−0.36	4.47587	4.82760
0.006	1.215	2.25	4.47668	4.82757
0.008	1.168	3.53	4.47567	4.82751
0.010	1.145	4.35	4.47671	4.82746
0.012	1.149	5.74	4.47560	4.82743

Table 15 The secondary parameters of aq-GO at 308.15 K

Conc. (g% w/v)	σ (10^{-2})	ϕ (10^{-3})	$K_{S\phi}$ (10^{-7})	V_{ϕ} (10^{4})
0.002	0.998	2.33	4.35555	4.842230
0.004	1.002	4.05	4.35577	4.842119
0.006	1.004	4.76	4.35543	4.842141
0.008	1.001	3.73	4.35547	4.842045
0.010	1.014	8.76	4.35540	4.842042
0.012	1.016	9.76	4.35529	4.841974

Table 16 Molar parameters of GO at 288.15 K[a]

Molality (10^{-6})	η_m (10^{6})	γ_m (10^{7})	σ_m (10^{4})	ρ_m (10^{6})	ϕ_m (10^{3})	KS_{ϕ_m}	V_{ϕ_m} (10^{4})	μ_m (10^{9})
0.41654	2.7502	18.34	3.6002	2.398565	6.7832	1.1173	3.13	3.5208
0.83329	1.3826	9.17	1.8099	1.198979	6.1514	0.5585	2.89	1.7600
1.25003	0.9251	6.11	1.2111	0.799257	5.3282	0.3722	3.21	1.1733
1.66682	0.7037	4.58	0.9212	0.599410	7.4837	0.2792	2.95	0.8799
2.08360	0.5682	3.67	0.7438	0.479515	7.8266	0.2233	2.89	0.7039
2.49852	0.4705	3.06	0.6159	0.399886	5.3663	0.1862	2.97	0.5871

[a] Symbol: η_m = molar viscosity (mPa s mol^{-1}), γ_m = molar surface tension (mN m^{-1} mol^{-1}), σ_m = molar friccohesity (scm^{-1} mol^{-1}), ρ_m = molar density (g cm^{-3} mol^{-1}), ϕ_m = molar fractional volume (cm^3 mol^{-1}) KS_{ϕ_m} = molar isentropic compressibility (10^{-1} cm s^2 mol^{-1}), μ_m = molar sound velocity (ms^{-1} mol^{-1}), V_{ϕ_m} = apparent molar volume (cm^3 mol^{-1}).

Table 17 Molar parameters of GO at 298.15 K

Molality (10^{-6})	η_m (10^{6})	γ_m (10^{7})	σ_m (10^{4})	ρ_m (10^{6})	ϕ_m (10^{3})	KS_{ϕ_m}	V_{ϕ_m} (10^{4})	μ_m (10^{9})
0.41654	2.1247	17.45	2.9226	2.393670	−5.8175	1.0747	3.8617	3.5935
0.83329	1.0676	9.10	1.4082	1.196531	−0.4322	0.5371	3.3790	1.7964
1.25003	0.7163	5.90	0.9718	0.797626	1.7971	0.3581	3.3791	1.1974
1.66682	0.5389	4.61	0.7007	0.598188	2.1152	0.2685	3.0171	0.8981
2.08360	0.4320	3.77	0.5494	0.478538	2.0857	0.2149	2.9447	0.7184
2.49852	0.3615	3.15	0.4598	0.399071	2.2974	0.1791	3.0158	0.5991

Table 18 Molar parameters of GO at 308.15 K

Molality (10^{-6})	η_m (10^{6})	γ_m (10^{8})	σ_m (10^{4})	ρ_m (10^{6})	ϕ_m (10^{3})	KS_{ϕ_m}	V_{ϕ_m} (10^{4})	μ_m (10^{9})
0.41654	1.7364	1.74	2.3955	2.386465	5.5936	1.0457	4.1134	3.6486
0.83329	0.8717	0.87	1.2025	1.192939	4.8544	0.5227	2.5347	1.8237
1.25003	0.5821	0.58	0.8030	0.795226	3.8103	0.3484	3.3849	1.2158
1.66682	0.4355	0.44	0.6007	0.596392	2.2402	0.2613	2.7171	0.9118
2.08360	0.3527	0.35	0.4865	0.477097	4.2021	0.2090	3.0450	0.7294
2.49852	0.2948	0.29	0.4067	0.397872	3.9058	0.1743	2.8169	0.6083

Author contributions

Krishan Kumar has conducted the bench work, calculations, plotting figures and other designing for effective discussion and conclusive. Riddhi P. Dave has conducted the bench work, calculations, plotting figures and other designing for effective discussion and conclusive. Sachin Dev has discussed the systems to be taken up for research work for designing effective discussion. Prof. Man Singh is over supervision for conducting the research work, frequent discussions, exploring new models outer experiment observations and matching with the explored scientific exhalations to substantially create the new science out of the research.

Conflicts of interest

The authors confirm that there is no conflict of interest.

Acknowledgements

The authors are thankful to the Central University of Gujarat, India, for facilities, the National Forensic Science University, India, for FT-IR analysis. Krishan Kumar and Riddhi P. Dave are thankful to Kuldeep Delu and Dr C. P. Bhasin for support.

References

1 T. A. Saleh, Protocols for synthesis of nanomaterials, polymers, and green materials as adsorbents for water treatment technologies, *Environ. Technol. Innovation*, 2021, **24**, 101821.
2 S. S. Maktedar, G. Avashthi and M. Singh, Ultrasound assisted simultaneous reduction and direct functionalization of graphene oxide with thermal and cytotoxicity profile, *Ultrason. Sonochem.*, 2017, **34**, 856–864.
3 A. Chandra, P. Malik, S. Singh, A. Roy, N. Sahoo and M. Singh, Sustainable research methodology for potassium nitrate recovery from seawater, *Chem. Eng. Process.*, 2022, **174**, 108870.
4 S. Dev and M. Singh, Metallic sulfide nanoparticles anchored graphene oxide: Synthesis, characterization and reduction of methylene blue to leuco methylene blue in aqueous mixtures, *J. Phys. Chem. Solids*, 2020, **139**, 109335.
5 R. Kumari and M. Singh, Photocatalytic reduction of fluorescent dyes in sunlight by newly synthesized spiroindenoquinoxaline pyrrolizidines, *ACS Omega*, 2020, **5**, 23201–23218.
6 G. Avashthi and M. Singh, Ultrasound accelerated near-edge functionalized heterogeneous graphene oxide sonocatalyst for surface optical bandwidth efficacy and *in situ* sonothermocatalysis, *New J. Chem.*, 2021, **45**, 5463–5483.
7 L. Utracki and R. Simha, Molecular weight and temperature dependence of intrinsic viscosities in very poor solvents, *J. Phys. Chem.*, 1963, **67**, 1056–1061.
8 M. P. J. Dohmen, A. M. Pereira, J. M. K. Timmer, N. E. Benes and J. T. F. Keurentjes, Hydrodynamic Radii of Polyethylene Glycols in Different Solvents Determined from Viscosity Measurements, *J. Chem. Eng. Data*, 2008, **53**, 63–65.
9 R. Sadeghi and M. T. Zafarani-Moattar, Thermodynamics of aqueous solutions of polyvinylpyrrolidone, *J. Chem. Thermodyn.*, 2004, **36**, 665–670.
10 K. Ito and T. Ukai, Determination of mark–houwink–sakurada constants for measurements of the molecular weights by gel permeation chromatography i. on the generalization of mathematical procedure, *Polym. J.*, 1986, **18**, 593–600.
11 M. A. Masuelli, Mark–Houwink Parameters for Aqueous-Soluble Polymers and Biopolymers at Various Temperatures, *J. Polym. Biopolym. Phys. Chem.*, 2014, **2**, 37–43.
12 M. S. A. Sher Shah, A. R. Park, K. Zhang, J. H. Park and P. J. Yoo, Green synthesis of biphasic TiO 2-reduced graphene oxide nanocomposites with highly enhanced photocatalytic activity, *ACS Appl. Mater. Interfaces*, 2012, **4**, 3893–3901.
13 R. K. Singh, R. Kumar and D. P. Singh, Graphene oxide: Strategies for synthesis, reduction and frontier applications, *RSC Adv.*, 2016, **6**, 64993–65011.
14 Y. Xu, J. Li and W. Huang, Porous graphene oxide prepared on nickel foam by electrophoretic deposition and thermal reduction as high-performance supercapacitor electrodes, *Materials*, 2017, **10**, 936.
15 P. Nemes-Incze, Z. Osváth, K. Kamarás and L. P. Biró, Anomalies in thickness measurements of graphene and few layer graphite crystals by tapping mode atomic force microscopy, *Carbon*, 2008, **46**, 1435–1442.
16 A. T. Abdel-Motagaly, W. M. A. El Rouby, S. I. El-Dek, I. M. El-Sherbiny and A. A. Farghali, Fast technique for the purification of as-prepared graphene oxide suspension, *Diamond Relat. Mater.*, 2018, **86**, 20–28.
17 C. J. Shearer, A. D. Slattery, A. J. Stapleton, J. G. Shapter and C. T. Gibson, Accurate thickness measurement of graphene, *Nanotechnology*, 2016, **27**, 125704.
18 M. Bera, Chandravati, P. Gupta and P. K. Maji, Facile one-pot synthesis of graphene oxide by sonication assisted mechanochemical approach and its surface chemistry, *J. Nanosci. Nanotechnol.*, 2018, **18**, 902–912.
19 J. Chen, Y. Li, L. Huang, C. Li and G. Shi, High-yield preparation of graphene oxide from small graphite flakes *via* an improved Hummers method with a simple purification process, *Carbon*, 2015, **81**, 826–834.
20 A. Kaniyoor and S. Ramaprabhu, A Raman spectroscopic investigation of graphite oxide derived graphene, *AIP Adv.*, 2012, **2**, 032183.
21 M. Singh, and S. Singh, *Survismeter: Fundamentals, Concepts, and Applications*, 1st edn, Jenny Stanford Publishing, DOI: **10.1201/9780429027611**, 2019.
22 Z. Yang, H. Peng, W. Wang and T. Liu, Crystallization behavior of poly(ε-caprolactone)/layered double hydroxide nanocomposites, *J. Appl. Polym. Sci.*, 2010, **116**, 2658–2667.
23 I. Castilla-Cortázar, A. Vidaurre, B. Marí and A. J. Campillo-Fernández, Morphology, crystallinity, and molecular weight of poly(ε-caprolactone)/graphene oxide hybrids, *Polymers*, 2019, **11**, 1099.
24 M. Singh, Survismeter - Type I and II for surface tension, viscosity measurements of liquids for academic, and research and development studies, *J. Biochem. Biophys. Methods*, 2006, **67**, 151–161.
25 G. Avashthi, S. S. Maktedar and M. Singh, Surface-Induced *in Situ* Sonothermodynamically Controlled Functionalized Graphene Oxide for *in vitro* Cytotoxicity and Antioxidant Evaluations, *ACS Omega*, 2019, **4**, 16385–16401.
26 S. R. Pandya and M. Singh, Dispersion and optical activities of newly synthesized magnetic nanoparticles with organic acids and dendrimers in DMSO studied with UV/vis spectrophotometry, *J. Mol. Liq.*, 2015, **211**, 146–156.
27 Y. Liu, B. Chen, D. Wang, N. Jiang, J. Tan, J. Fu, B. Wu, Y. Hu and Z. Guo, Surface tension of supercooled graphene oxide nanofluids measured with acoustic levitation, *J. Therm. Anal. Calorim.*, 2021, **144**, 1369–1379.
28 D. Cabaleiro, P. Estellé, H. Navas, A. Desforges and B. Vigolo, Dynamic viscosity and surface tension of stable graphene

oxide and reduced graphene oxide aqueous nanofluids, *J. Nanofluids*, 2018, **7**, 1081–1088.

29 S. U. Ilyas, S. Ridha and F. A. Abdul Kareem, Dispersion stability and surface tension of SDS-Stabilized saline nanofluids with graphene nanoplatelets, *Colloids Surf., A*, 2020, **592**, 124584.

30 A. Kujawska, R. Mulka, S. Hamze, G. Żyła, B. Zajaczkowski, M. H. Buschmann and P. Estellé, The effect of boiling in a thermosyphon on surface tension and contact angle of silica and graphene oxide nanofluids, *Colloids Surf., A*, 2021, **627**, 127082.

31 S. S. Maktedar, P. Malik, G. Avashthi and M. Singh, Dispersion enhancing effect of sonochemically functionalized graphene oxide for catalysing antioxidant efficacy of curcumin, *Ultrason. Sonochem.*, 2017, **39**, 208–217.

32 R. Kamatchi, S. Venkatachalapathy and B. A. Srinivas, International Journal of Thermal Sciences Synthesis , stability , transport properties , and surface wettability of reduced graphene oxide/water nano fl uids, *Int. J. Therm. Sci.*, 2015, **97**, 17–25.

33 H. Karami, S. Papari-Zare, M. Shanbedi, H. Eshghi, A. Dashtbozorg, A. Akbari, E. Mohammadian, M. Heidari, A. Z. Sahin and C. B. Teng, The thermophysical properties and the stability of nanofluids containing carboxyl-functionalized graphene nano-platelets and multi-walled carbon nanotubes, *Int. Commun. Heat Mass Transfer*, 2019, **108**, 104302.

34 A. Bakak, M. Lotfi, R. Heyd, A. Ammar and A. Koumina, Viscosity and Rheological Properties of Graphene Nanopowders Nanofluids, *Entropy*, 2021, **23**, 979.

35 F. Jabbari, A. Rajabpour and S. Saedodin, Viscosity of carbon nanotube/water nanofluid: Equilibrium molecular dynamics, *J. Therm. Anal. Calorim.*, 2019, **135**, 1787–1796.

36 A. Ansón-Casaos, J. C. Ciria, O. Sanahuja-Parejo, S. Víctor-Román, J. M. González-Domínguez, E. García-Bordejé, A. M. Benito and W. K. Maser, The viscosity of dilute carbon nanotube (1D) and graphene oxide (2D) nanofluids, *Phys. Chem. Chem. Phys.*, 2020, **22**, 11474–11484.

37 D. Cabaleiro, L. Colla, S. Barison, L. Lugo, L. Fedele and S. Bobbo, Heat Transfer Capability of (Ethylene Glycol + Water)-Based Nanofluids Containing Graphene Nanoplatelets: Design and Thermophysical Profile, *Nanoscale Res. Lett.*, 2017, **12**, DOI: **10.1186/s11671-016-1806-x**.

38 S. S. Maktedar, P. Malik, G. Avashthi and M. Singh, Dispersion enhancing effect of sonochemically functionalized graphene oxide for catalysing antioxidant efficacy of curcumin, *Ultrason. Sonochem.*, 2017, **39**, 208–217.

39 M. Mehrali, E. Sadeghinezhad, A. R. Akhiani, S. Tahan Latibari, H. S. C. Metselaar, A. S. Kherbeet and M. Mehrali, Heat transfer and entropy generation analysis of hybrid graphene/Fe_3O_4 ferro-nanofluid flow under the influence of a magnetic field, *Powder Technol.*, 2017, **308**, 149–157.

40 H. Yarmand, S. Gharehkhani, S. F. S. Shirazi, A. Amiri, M. S. Alehashem, M. Dahari and S. N. Kazi, Experimental investigation of thermo-physical properties, convective heat transfer and pressure drop of functionalized graphene nanoplatelets aqueous nanofluid in a square heated pipe, *Energy Convers. Manage.*, 2016, **114**, 38–49.

41 M. Mehrali, E. Sadeghinezhad, S. T. Latibari, S. N. Kazi, M. Mehrali, M. Nashrul, B. Mohd, H. Simon and C. Metselaar, Investigation of thermal conductivity and rheological properties of nanofluids containing graphene nanoplatelets, *Nanoscale Res. Lett.*, 2014, **9**, 15.

42 A. A. Farajian, R. Mortezaee, T. H. Osborn, O. V. Pupysheva, M. Wang, A. Zhamu and B. Z. Jang, Multiscale molecular thermodynamics of graphene-oxide liquid-phase exfoliation, *Phys. Chem. Chem. Phys.*, 2019, **21**, 1761–1772.

43 S. Pandit and M. De, Interaction of Amino Acids and Graphene Interaction of Amino Acids and Graphene Oxide, *J. Phys. Chem. C*, 2017, **121**, 600.

44 H. L. Zhang and S. J. Han, Viscosity and density of water + sodium chloride + potassium chloride solutions at 298.15 K, *J. Chem. Eng. Data*, 1996, **41**, 516–520.

45 S. S. Maktedar, G. Avashthi and M. Singh, Understanding the significance of O-doped graphene towards biomedical applications, *RSC Adv.*, 2016, **6**, 114264–114275.

46 S. S. Maktedar, S. S. Mehetre, G. Avashthi and M. Singh, In situ sonochemical reduction and direct functionalization of graphene oxide: A robust approach with thermal and biomedical applications, *Ultrason. Sonochem.*, 2017, **34**, 67–77.